



저작자표시-비영리-변경금지 2.0 대한민국

이용자는 아래의 조건을 따르는 경우에 한하여 자유롭게

- 이 저작물을 복제, 배포, 전송, 전시, 공연 및 방송할 수 있습니다.

다음과 같은 조건을 따라야 합니다:



저작자표시. 귀하는 원저작자를 표시하여야 합니다.



비영리. 귀하는 이 저작물을 영리 목적으로 이용할 수 없습니다.



변경금지. 귀하는 이 저작물을 개작, 변형 또는 가공할 수 없습니다.

- 귀하는, 이 저작물의 재이용이나 배포의 경우, 이 저작물에 적용된 이용허락조건을 명확하게 나타내어야 합니다.
- 저작권자로부터 별도의 허가를 받으면 이러한 조건들은 적용되지 않습니다.

저작권법에 따른 이용자의 권리는 위의 내용에 의하여 영향을 받지 않습니다.

이것은 [이용허락규약\(Legal Code\)](#)을 이해하기 쉽게 요약한 것입니다.

[Disclaimer](#)

공학박사 학위논문

**Development of hybrid process using
laser and dry particle
deposition system**

레이저와 건식 분말 적층 장치를 사용한
하이브리드 공정 개발

2016년 8월

서울대학교 대학원

기계항공공학부

최 정 오

Abstract

Development of hybrid process using laser and dry particle deposition system

Jung-Oh Choi

Department of Mechanical and Aerospace Engineering

The Graduate School

Seoul National University

A nanoparticle deposition system (NPDS) was developed as an alternative to aerosol deposition, with advantages including cold spray (room temperature) processing, the use of various materials (metal and ceramic), high deposition rates (versus molecular and atomic deposition), and a green manufacturing process with no wet chemical processing, binder, or post-processing step. This NPDS was shown to be useful in the deposition of particles on soft matter for flexible substrate applications.

With the aim of enhancing adhesion between the film and the fabricated substrate in NPDS, a laser was used initially on flying nanoparticles, referred to as laser-assisted NPDS (LaNPDS). In other fabrication methods, the laser has been used to shape objects by sintering and melting target materials. In contrast, a coherent laser can transfer thermal energy inside the tube to flying nanoparticles and deposited nanoparticles, without thermal damage, for the fusion and dissolution of substrates. This indicates that thermal energy transfer plays a role in preheating, with an increase in the diffusion rate at the interface between nanoparticles, resulting in

enhanced necking phenomena over the mechanism of solid-state sintering. Given this, LaNPDS was expected to improve not only surface integrity, but also adhesion among nanoparticles in the film, as well as the interfaces between the film and substrate. However, the intrinsic role of the laser in relation to surface integrity and adhesion has not been reported previously, so the effect of laser irradiation was examined in this study.

In this study, Al_2O_3 and TiO_2 ceramic particles were deposited on ceramic (sapphire) and polymer substrates (PET and ITO-PET) by LaNPDS. The surface morphology, hardness, elastic modulus, and interface were characterized by field emission scanning electron microscopy (FE-SEM), surface profile, nano indentation, and X-ray diffraction (XRD). To demonstrate the heating effect and changes in the mechanical properties of ceramic films, as influenced by the laser, a finite-element method was used.

Using LaNPDS, applications of this research include fabricated dye-sensitized solar cells (DSSCs) and electrochromic windows (ECWs). As the intensity of the laser was increased, the efficiencies of the DSSCs and ECWs increased.

Flying particle velocity was analyzed by a computational fluid dynamics (CFD) method and a microparticle image velocimetry (micro-PIV) method. Through these measurements, the effects of the laser on flying particles were analyzed. The flying particle kinetic energy and laser activation energy were calculated and compared with a CFD analysis. The laser activation energy added to the kinetic energy, so the total impact energy increased. From these results, the LaNPDS process can deposit ceramic materials on various substrates more effectively, because the laser energy is transferred to the flying nanoparticles.

Keywords: laser, Nano particle deposition system (NPDS), Ceramic particle deposition, Room temperature, Atmospheric pressure, Dye-sensitized solar cell (DSSC), Flexible substrate

Student Number: 2010-20725

Contents

Chapter 1 Introduction	1
1.1. Overview	1
1.2. Review of particle deposition methods	1
1.2.1. History of low temperature deposition processes	2
1.2.2. Nano particle deposition system (NPDS).....	4
1.3. Review of laser assisted sintering process.....	4
1.3.1. Classification of laser assisted sintering methods.....	6
1.3.2. Limitation of existing laser assisted deposition process	8
1.3.3 Approaches for a laser assisted hybrid process.....	9
Chapter 2 System design and configuration	10
2.1. System configuration.....	10
2.2. Direct laser method	11
2.3. In-direct laser method.....	13
Chapter 3 Evaluation of deposition results	14
3.1. Overview	14
3.2. Al ₂ O ₃ ceramic particle deposition.....	17
3.2.1. Direct laser method results	19
3.3. TiO ₂ particle deposition.....	25
3.3.1. Direct laser method results	26
3.3.2. In-direct laser method results.....	29
Chapter 4 Effect of laser on flying particle.....	32
4.1. Overview	32
4.2. Evaluation of laser effect on flying particle	33

4.3. Particle velocity measurement	38
4.3.1. Hardware set up of micro PIV system.....	40
4.3.2. Measurement of Zn particle velocity	43
4.4. Computational fluid dynamics.....	47
4.4.1 CFD modeling.....	49
4.4.2. CFD analysis.....	50
Chapter 5 Applications.....	53
5.1. Overview	53
5.2. Fabrication and evaluation of Dye Sensitized Solar Cell (DSSC) and Electro Chromic Window (ECW).....	54
Chapter 6 Bonding mechanism	61
6.1. Overview	61
6.2. Particle heating in coaxial laser	62
6.3. Thermal effect of laser in LaNPDS.....	63
6.4. Relationships between the kinetic energy of the particles and laser activation energy in LaNPDS.....	66
6.4.1 ANSYS modeling for particle velocity	66
6.4.2 Laser activation energy.....	72
6.4.3 Comparison of kinetic energy and laser activation energies	74
Chapter 7 Conclusions	76
Bibliography	77
Abstract	85

List of Tables

Table 1 Classification of laser assisted sintering methods	7
Table 2 Deposition process parameters	18
Table 3 Experiment conditions	19
Table 4 Flying particle conditions.....	32
Table 5 CFD analysis condition	48
Table 6 Results of simulation and PIV measurement.....	52
Table 7 Activation energy of Al ₂ O ₃ particle sintering condition	72

List of Figures

Figure 1 Particle deposition method.....	2
Figure 2 History of low temperature deposition processed.....	3
Figure 3 Nano Particle Deposition System (NPDS)	4
Figure 4 Laser assisted sintering methods.....	6
Figure 5 Damage on the ITO-PET substrate	8
Figure 6 Direct laser method	11
Figure 7 Figure of direct laser method	12
Figure 8 In-direct laser method.....	13
Figure 9 LaNPDS hard ware set up.....	13
Figure 10 Aggregated TiO ₂ particle, single particle size 15 nm	15
Figure 11 Al ₂ O ₃ particles < 1µm.....	15
Figure 12 Schematic diagram of light spectrophotometer	16
Figure 13 TiO ₂ and Al ₂ O ₃ particle light absorbance result.....	16
Figure 14 SEM image of Al ₂ O ₃ particle	17
Figure 15 Schematic diagram of deposition process.....	19
Figure 16 Film thickness of Al ₂ O ₃ deposition on various substrate	20
Figure 17 Film roughness of Al ₂ O ₃ deposition on various substrate	21
Figure 18 Mechanical properties of Al ₂ O ₃ deposition results - Direct laser method	22
Figure 19 Schematic diagram of nano indentation method.....	22
Figure 20 XRD results of Al ₂ O ₃ deposition results - Direct laser method.....	24
Figure 21 SEM image of TiO ₂ particle.....	25

Figure 22 The pros and cons of direct laser method	26
Figure 23 SEM image of TiO ₂ deposition result by direct laser method.....	27
Figure 24 Mechanical properties of TiO ₂ deposition result.....	28
Figure 25 SEM image of deposited TiO ₂ surface morphology.....	29
Figure 26 SIM image of cross section of TiO ₂ film fabricate.....	30
Figure 27 Thickness result of deposited TiO ₂ particle	31
Figure 28 Indentation result of deposited TiO ₂	31
Figure 29 Schematic diagram of laser and particle mixed tube.....	32
Figure 30 Schematic diagram of flying particle capturing experiment set up	33
Figure 31 Figure of inner mesh and captured Al ₂ O ₃ results	34
Figure 32 FE-SEM image of captured flying Al ₂ O ₃ particle.....	35
Figure 33 XRD measurement results of captured flying Al ₂ O ₃ particle.....	37
Figure 34 Hardware set up of PIV system.....	41
Figure 35 Figure of micro PIV system.....	41
Figure 36 Figure of transparent window for flying particle observation (A) only laser turn on condition, (B) laser turn on with flying particle.....	42
Figure 37 SIM image of Zn particle for PIV	43
Figure 38 Referencing for size measurement	43
Figure 39 Particle size and velocity measurement.....	44
Figure 40 Captured Zn flying particle in 5 msec	44
Figure 41 Zn particle velocity result - no laser power	45
Figure 42 Zn particle velocity result - laser power 500 mW	46

Figure 43 Geometry and boundary conditions for simulation.....	49
Figure 44 Air flow simulation result	51
Figure 45 Particle velocity simulation result	52
Figure 46 Schematic diagram of Dye Sensitized Solar Cell	53
Figure 47 Flexible DSSC fabricated by LaNPDS.....	55
Figure 48 DSSC efficiency result - In-direct laser method	56
Figure 49 DSSC efficiency result - Direct laser method.....	56
Figure 50 Background of ECW	57
Figure 51 FE-SEM image of cross section of the CeO ₂ film on FTO glass.....	58
Figure 52 Applied voltage change and transmittance change over cycle test.....	58
Figure 53 Transmittance result of without laser condition	59
Figure 54 Transmittance result of with laser condition.....	60
Figure 55 Map of phenomena that occur during deposition.....	62
Figure 56 Schematic diagram of laser energy irradiation of flying particles	64
Figure 57 Calculated temperature of flying particle in a laser- assisted nanoparticle deposition system (LaNPDS)	65
Figure 58 Image of slit shape nozzle.....	67
Figure 59 Geometry information of CFD analysis modeling.....	68
Figure 60 Contour image of CFD results about air and particle flow velocity.....	69
Figure 61 Velocity result of computational fluid dynamics (CFD) analysis.....	70
Figure 62 Velocity result of CFD analysis in region A	71
Figure 63 Kinetic energy and laser activation energies.....	74

Figure 64 Comparison of kinetic and laser activation energies.....75

Chapter 1 Introduction

1.1. Overview

Nano particle deposition system (NPDS), is a metal and ceramic deposition process, spraying nano or micro sized particles under low temperature and low vacuum conditions [1-3], was used to deposit the semiconductor oxide powders by a dry-spray method. NPDS is similar to other coating processes, such as thermal-spray [4], gas deposition method (GDM) [5], hypersonic plasma particle deposition (HPPD) [6], electrostatic particle impact deposition (EPID) [7], cold spray, and aerosol deposition methods (ADM).

1.2. Review of particle deposition methods

Although cold-spray and ADM can be used to coat at room temperature, both processes support only a limited specific velocity and powder size, so the powder type and the deposition substrates are limited.

For the enhancement of particle bonding, external energy added on the particle deposition method. Cold spray method added the laser for pre-heating, called laser assisted cold spray (LaCD). LaCD uses laser for pre-treatment on the substrate. Laser focused on the surface of substrate. After substrate pre-heated than particle deposited through the nozzle.

Selective laser sintering (SLS) and laser engineered net shaping use in a different way. These process use high power laser, laser beam is focus on the substrate directly.

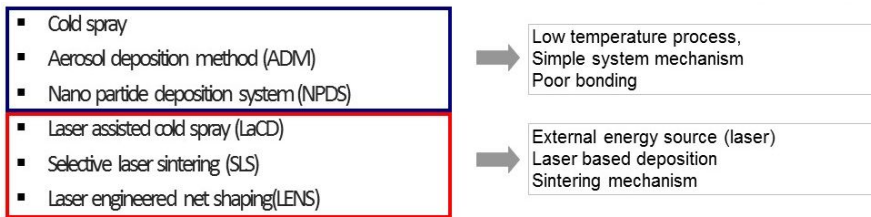


Figure 1 Particle deposition method

1.2.1. History of low temperature deposition processes

Cold spray deposition developed in early 1980s [8], unlike the name shown, process temperature is not cold. Normally CD deposit the metal particle at around 500 °C. This process accelerates powder particles, generally metals and cermet powder, through a supersonic nozzle using heated gas or helium, and the powder particles are sprayed onto a substrate. The kinetic energy of the particles impacting on the substrate is used for bonding.

The aerosol deposition method (ADM) is a new room-temperature process for ceramic coating developed by Dr. Akedo in late 1990s [9-11]. This process involves aerosol generation, particle impact, and deposition on the substrate. It uses the aerosol state of submicron particles to accelerate ultrafine particles and mix them in gas flow. Aerosol with particles is accelerated by a gas flow in the nozzle and sprayed onto the substrate. The kinetic energy of the particles is used for bonding during the impact.

NPDS was developed in 2006 by Chun and Ahn [1, 2], to fabricate metal and ceramic film by spraying nano/micro sized particles at room temperature under low vacuum condition. The system consists of a compressor for carrier gas, powder feeders, nozzles, a vacuum chamber, a vacuum pump, and controllers. The compressor supplies the pressurized air that carries particles from the powder feeders to the supersonic nozzles. The particles are sprayed through the nozzle at room temperature under the low vacuum condition and they are impacted onto the substrate.

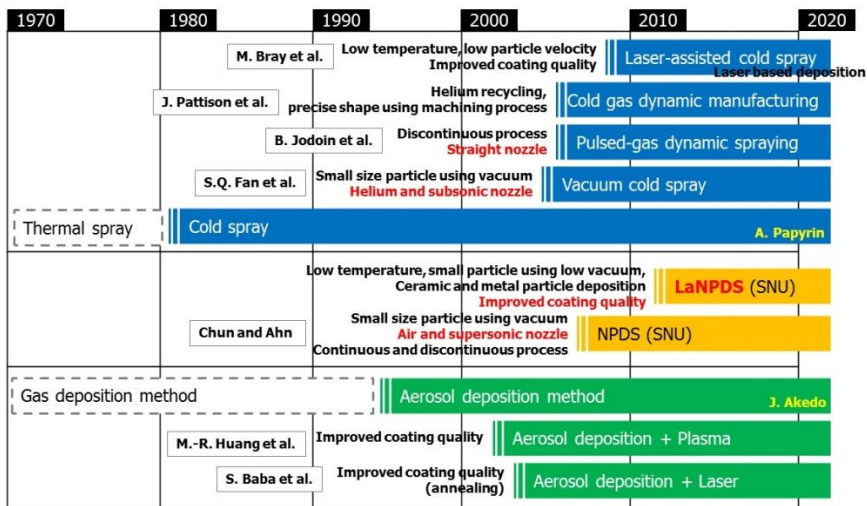


Figure 2 History of low temperature deposition processed

1.2.2. Nano particle deposition system (NPDS)

NPDS could make thin coating layer through dry-spray method under low vacuum and low temperature condition. As shown in Figure 3, NPDS consists of controller, deposition chamber with substrate holder and nozzle, powder supplier, air compressor, and vacuum pump, etc. The pressure condition of deposition chamber was maintained in atmospheric pressure condition to increase the economic feasibility and productivity.

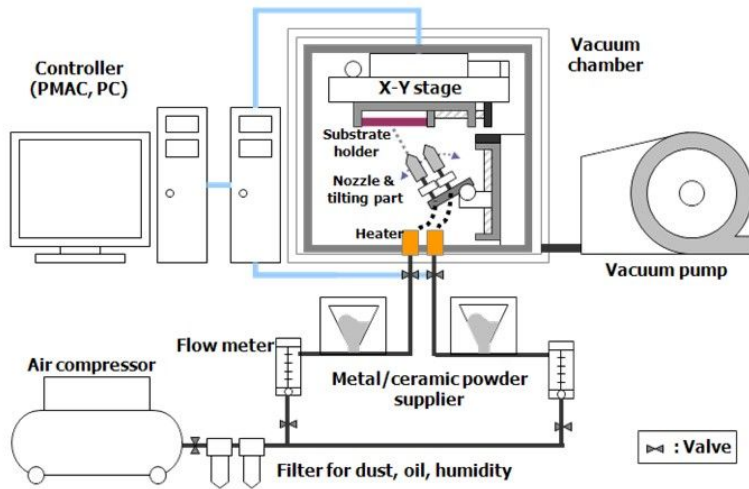


Figure 3 Nano Particle Deposition System (NPDS) [12]

1.3. Review of laser assisted sintering process

Photo curing is the basis of stereo lithography (SL), one of the most popular and most accurate solid freeform (SFF) techniques. Commercial SL machines (3D system, CA) produce plastic prototypes from epoxy resins by photopolymerization of a liquid monomer with a UV laser. For the 3D-fabrication of ceramics via SL the liquid monomer is replaced by ceramic resin, a suspension of ceramic powder dispersed in a UV-curable resin, first

demonstrated by Griffith and Halloran (Griffith & Halloran, 1996) [12]. As shown in Figure 4 - (a), the first step is curing a thin layer (150~200 μm) by laser scanning the cross section on the surface of the ceramic resin. The part is attached by supports to an elevator platform beneath the surface of the ceramic resin. After curing the layer, the elevator platform dips into the suspension allowing the liquid ceramic resin to flow over the cured portion of the part. A doctor blade sweeps over the surface leaving a layer of fresh ceramic suspension which becomes the next cured layer after the laser curing process. Repeating this process building up the three dimensional green body of the ceramic components. And then after post sintering in furnace, dense ceramic objects are obtained. Lasers used in current practice are helium cadmium gas lasers, argon ion gas laser and more recently solid state Nd-YVO₄ lasers [13].

To achieve a sufficiently high green density in the part, the solid volume fraction should be in the range of 0.50-0.65. On the other hand, a low viscosity is necessary for a proper flow during recoating of the next layer. Alumina and silica powders have been used to prepare the ceramic suspension [14]. Final mechanical strength similar with that of the uniaxial pressed samples has been achieved.

1.3.1. Classification of laser assisted sintering methods

Laser techniques Thermal spray and laser processing can be considered as half brothers since they show many common features due to the use of a (more or less) high-energy source for both (Jeandin et al., 2010) [15]. Their combination can therefore be very fruitful and prominent to achieve coatings, which results in their most recent and advanced applications. Laser thermal spray hybrid processes have been developed as a result of the successful combination of laser and thermal spray technologies. Various types of laser have been combined with the guns of thermal spray process. Combining laser processing to thermal spray resulted in a major improvement for thermal spray in 3 sub-areas, i.e. that of pretreatment, that of post-treatment and that of simulation of thermal and kinetic phenomena.

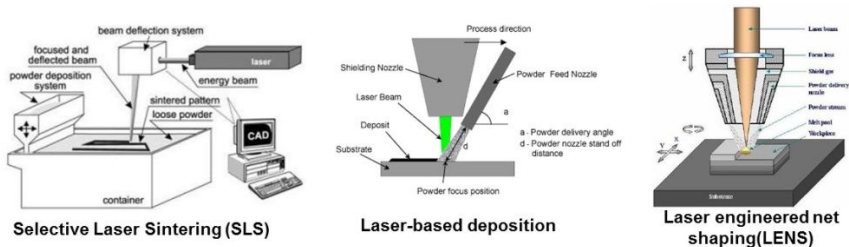


Figure 4 Laser assisted sintering methods [15-17]

Table 1 Classification of laser assisted sintering methods

	SLS	Laser based deposition	LENS
Sintering method	Solid state sintering	Partially melting	Full melting
Material	Ceramic, metal, glass	Ceramic, metal	Metal
Energy	High power laser (> 100 W)	High power laser (> 1,000 W)	High power laser (> 1,000 W)
Temperature	800 ~ 1,000 °C	1,000 ~ 1,400 °C	1,000 ~ 1,400 °C
Dimension	3-D	2-D	3-D
Layer thickness	16 ~ 50 mm	300 ~ 500 mm	100 ~ 400 mm
Research institute	University of Texas mid	Russian Academy of Science	Sandia National Laboratories

1.3.2. Limitation of existing laser assisted deposition process

Polymer substrates have been developed for use in flexible displays, organic devices, and other applications. These polymer substrates are very vulnerable to heat and can be easily damaged by a high process temperature. Nevertheless laser thermal hybrid process successfully fabricated metal and ceramic features, these process are not suitable for polymer substrate. Therefore, a new additive manufacturing process with low temperature is required for consider the low temperature at the surface of substrate.

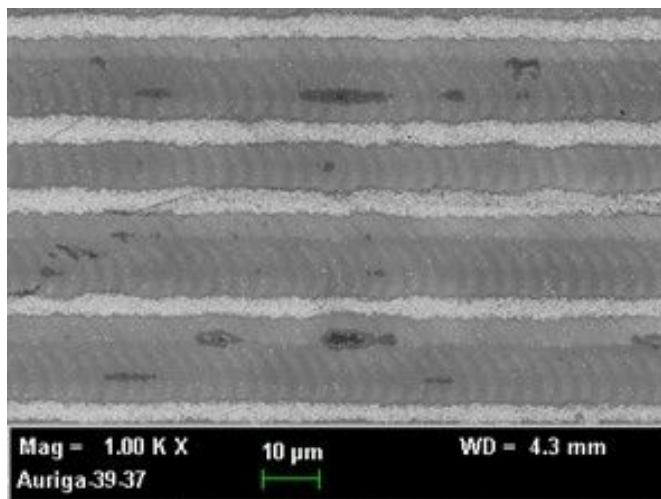


Figure 5 Damage on the ITO-PET substrate

1.3.3 Approaches for a laser assisted hybrid process

For the enhancement of adhesion between the film and the fabricated substrate in NPDS, the coherent laser beam had been initially utilized on flying nanoparticles through the path of particle flow in NPDS, called laser assisted NPDS (LaNPDS). LaNPDS process is different from the other fabrication methods, laser to shaping of object by sintering and melting the target materials has been used.

In contrary, the coherent laser can transfer thermal energy to the flying nanoparticles and deposited nanoparticles with minimum thermal damage as for a fusion and a dissolution of substrates. This infers that thermal energy transfer play is a role in preheating with an increment of diffusion rate at the interface between nanoparticles, resulting in enhanced necking phenomena over the mechanism of solid state sintering [14]. With this assumption, LaNPDS was expected to improve not only surface integrity and but also adhesion among nanoparticles in the film and the interfaces between the film and substrate. However, the intrinsic role of the laser in relation to the surface integrity and adhesion has not been reported and, so the effect of the laser irradiation was carried out in this study.

Chapter 2 System design and configuration

2.1. System configuration

The LaNPDS consists of an air compressor, powder feeders, nozzles, a vacuum chamber, a vacuum pump, and controllers. The air compressor provides the 0.3 MPa pressure airflow that carries particles from the powder feeder to the nozzle. The powder is sprayed through the nozzle at room temperature under low vacuum (> 25 Torr) conditions and deposited on the substrate. During this process, the powder flying was designed to meet the laser coaxial. In this system used a 355 nm UV pulsed laser. (Aptowave UV pulsed wave laser) laser has <4 W power at 30KHz and pulse with 15~10 ns at 30KHz.

2.2. Direct laser method

Configuration of the direct laser method can be shown in figure 5. The system consists of a laser source for ultra violet (UV) laser of wavelength 355 nm, laser scanning system, compressed air supplier, powder feeder, nozzle for accelerating particles, deposition chamber, vacuum pump, substrate holder and x-y stage for substrate positioning

In this system flying particle energizing and local sintering by laser in the nozzle. It can improve surface qualities of deposited film. But the reflected laser occurred damage on the substrate.

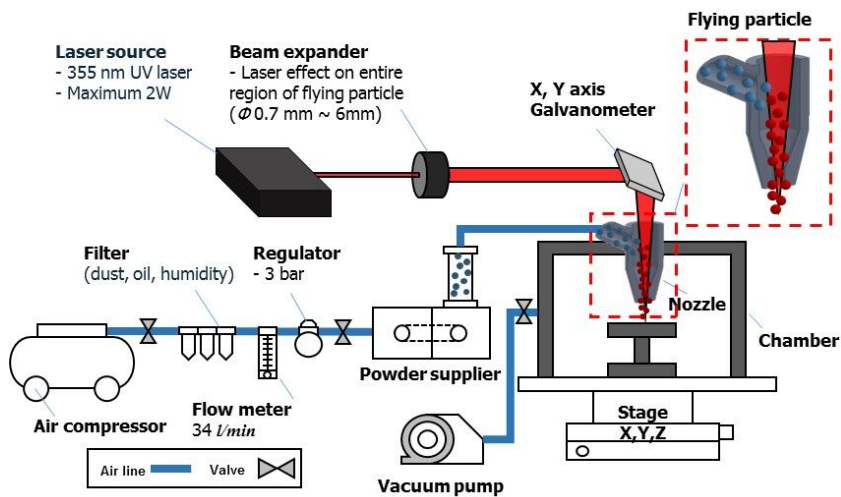


Figure 6 Direct laser method

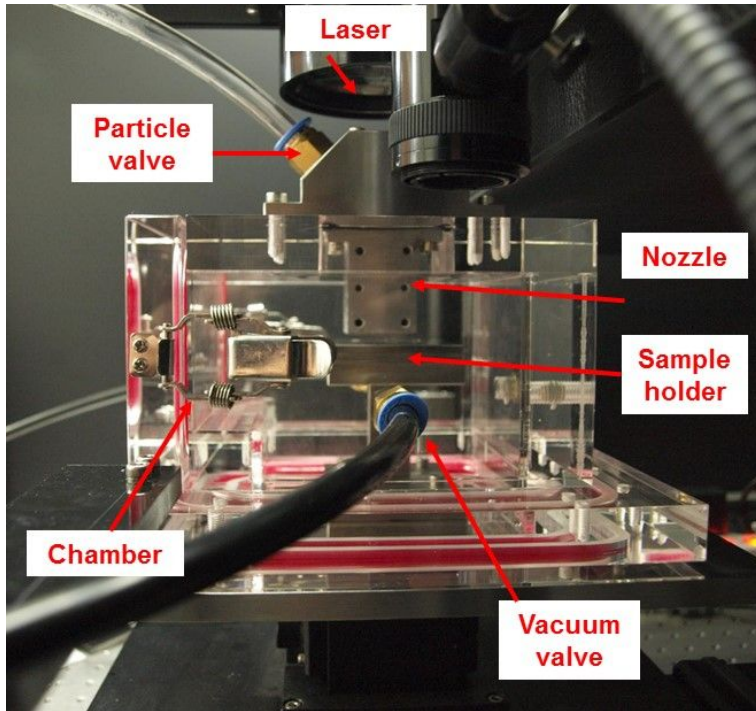


Figure 7 Figure of direct laser method

2.3. In-direct laser method

For the In-direct laser method, the configuration of system is almost same but little difference between the direct method. In the tube laser and flying particle flow coaxially and energized. Tube length can controlled. Initial laser beam has 1mm diameter, after pass the beam expander the laser diameter became 6~7 mm. in-direct laser method can control the amount of laser energy input and duration time. This method can eliminate the thermal damage on the substrate. Figure 7 shows hardware set-up of in-direct laser method.

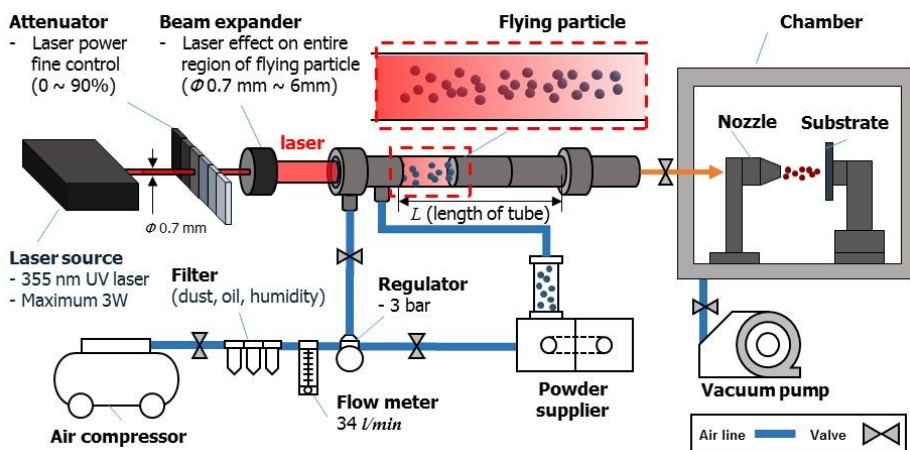


Figure 8 In-direct laser method

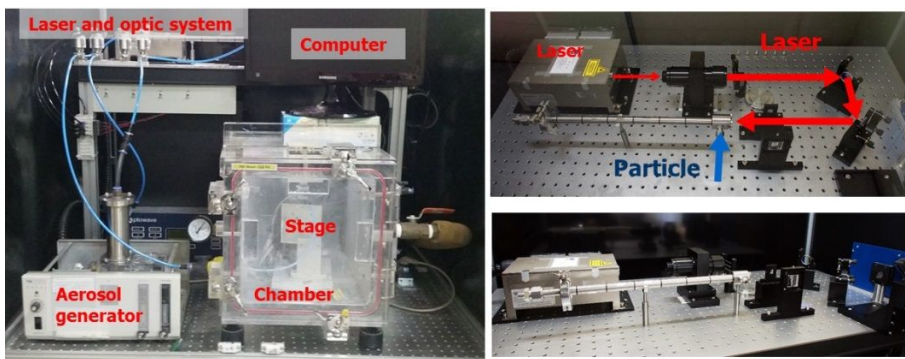


Figure 9 LaNPDS hard ware set up

Chapter 3 Evaluation of deposition results

3.1. Overview

In this chapter, the deposition result by LaNPDS were presented. The printing materials are selected with functional metal and ceramic materials. For ceramic printing TiO_2 and Al_2O_3 particle are chosen, TiO_2 is widely used for photo electrode. Among the various semiconductor oxide, titanium dioxide, TiO_2 , turned out to the most suitable in DSSC semiconductor oxide materials for realizing the highest solar energy efficiency.

As materials of thin film, ceramic nanoparticle of Al_2O_3 was selected owing to their wide applications. Al_2O_3 can be used as a hard surface, electrical insulator, dielectric layer for capacitor among other uses. In particular, Al_2O_3 has been widely researched for impact analysis and the material properties for impact analysis have been widely reported and was therefore deemed, for confirming the effect of laser in high speed impact of particles.

For the ceramic particle selection, relationship between the laser wavelength and material light absorption was considered. Figure 8 shows experiment detail about light absorption and figure 9 shows TiO_2 light absorption result. TiO_2 particle absorbs the 355 nm wavelength laser well.

For the metal deposition Zn and Sn were chosen. Sn has low melting temperature so it is widely used for the solder material and conductive material. Zn is used for conductive line. And used for particle velocity measurement.

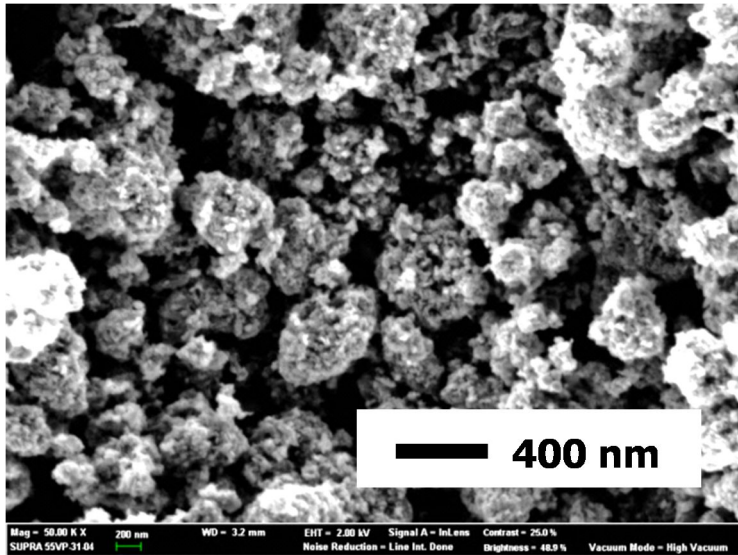


Figure 10 Aggregated TiO₂ particle, single particle size 15 nm

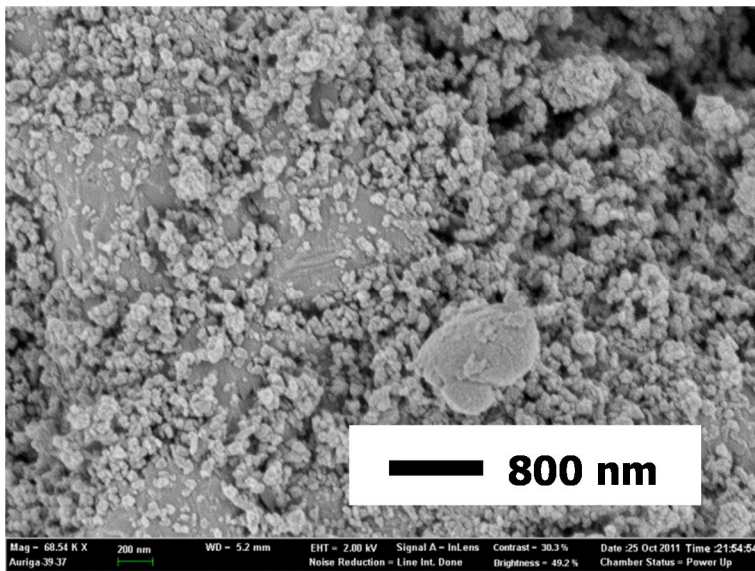


Figure 11 Al₂O₃ particles < 1 μ m

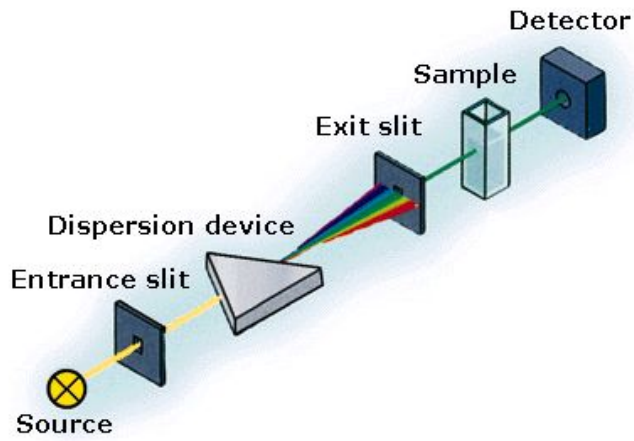


Figure 12 Schematic diagram of light spectrophotometer

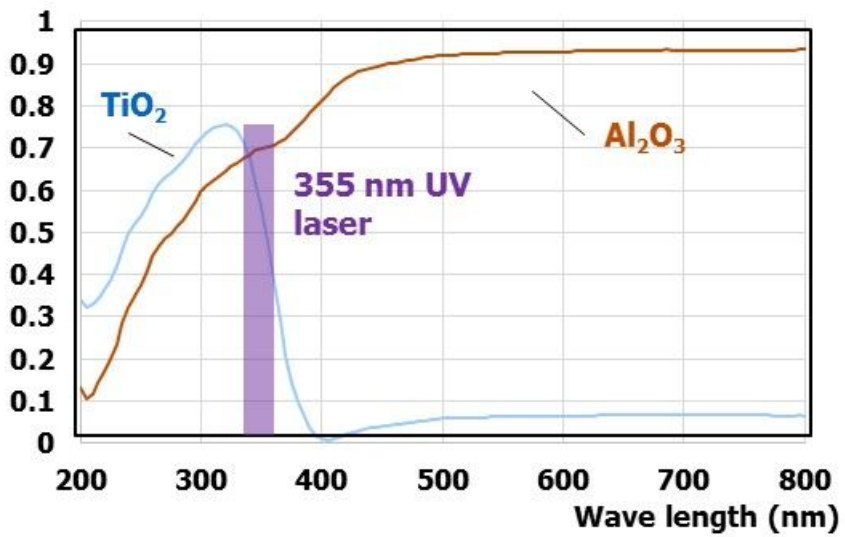


Figure 13 TiO_2 and Al_2O_3 particle light absorbance result

3.2. Al_2O_3 ceramic particle deposition

Alumina (Al_2O_3) is one of the most widely used ceramic materials as catalysts, catalyst supports and absorbents, and also wear resistant coating. Alumina is an electrical insulator but has a relatively high conductivity for a ceramic material. Being chemically inert and white, alumina is favored filler for plastics. Also, it is a common ingredient in sunscreen and lots of cosmetics. Alumina is used as a catalyst support for many industrial applications. The most common occurring crystalline form, alpha-phase alumina, makes it suitable for use as an abrasive and as a component in cutting tools. The other phases, gamma-m delta-, eta-, theta-, and chi-alumina are also existed [18].

Figure 11 shows size and shape of alumina used in this research. The size of alumina is $< 3\mu\text{m}$ and has spherical shape (Sigma Aldrich). Table 2 is deposition process parameters. Stage, nozzle stand-off distance, compressor pressure, temperature, chamber condition are same for direct/in-direct laser method. The difference is laser input type and laser power.

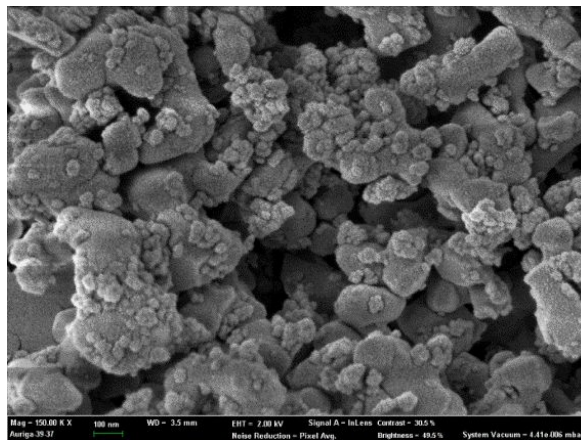


Figure 14 SEM image of Al_2O_3 particle

Table 2 Deposition process parameters

Parameters	Values
Stage speed (mm/s)	0.025
Stand-off distance (mm)	3
Compressor pressure (MPa)	0.4
Chamber pressure (MPa)	0.02 ~ 0.03
Flow rate (L/min)	6-12
Deposited shape	line, rectangular areas (10 mm × 3 mm , 10 mm × 10 mm)
Powder material	Al ₂ O ₃
Substrate materials	Al ₂ O ₃

3.2.1. Direct laser method results

As described earlier in direct laser method, laser focused on nozzle neck. So the laser pass through the nozzle and has effect on the substrate. For the deposition the nozzle has rectangular shape, the size of outlet is $0.4 \text{ mm} \times 10 \text{ mm}$. But laser has a circle shape at the focused surface. For cover the whole area of deposition, Galvano meter used. Laser moves rapidly to cover all the nozzle outlet. Figure 12 shows laser path and deposition process. And table 3 shows detail experiment conditions.

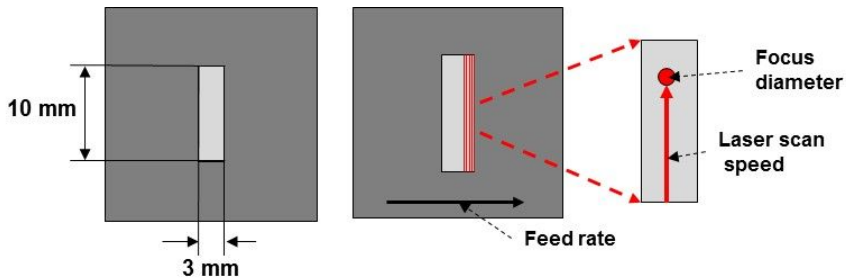


Figure 15 Schematic diagram of deposition process

Table 3 Experiment conditions

Laser	Laser type	355 nm UV laser
	Pulse width	<30 ns at 30 kHz
	Power	~ 25 mW
	Laser scan speed	100 mm/s
NPDS	Chamber pressure	0.02 MPa
	Compressed air	0.4 MPa
	Substrate	ITO-PET 15 ohm/sq. FTO-glass 15 ohm/sq.
Stage	Feed rate	0.025 mm/sec
	Stand-off distance	3 mm

Al_2O_3 powder was deposited on sapphire wafer for analysis of laser effect. The process parameters for laser assisted deposition were as following; the carrier gas pressure, the chamber vacuum pressure, the standoff distance and the feed rate were 0.4 MPa, 0.04 MPa, 3 mm and 0.025 mm/s. Then, five types (0, 4, 8, 15 and 25 mW) of laser power were applied on the flying nanoparticles in nozzle. Other laser condition was 30 kHz, 30 nsec, 100 mm/s for frequency, pulse duration and scan speed, respectively.

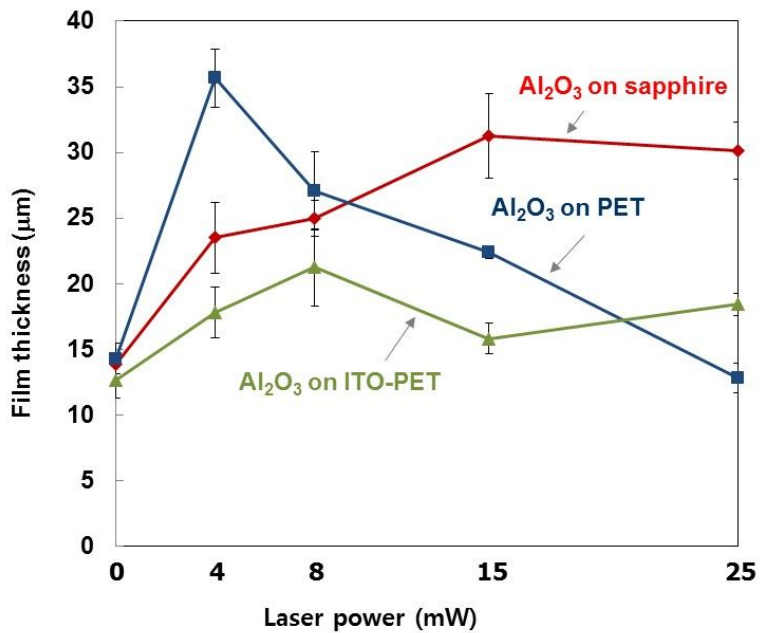


Figure 16 Film thickness of Al_2O_3 deposition on various substrate using direct laser method

The surface roughness and film thickness were measured by a Dektak 6M surface profiler (Veeco Instruments, Tucson, AZ, USA). The thickness on sapphire wafer was increased as the laser power increased. In addition, the nanoscale mechanical properties of Al_2O_3 film on sapphire substrate were measured by nanoindentation (MTS XP, MTS System Corporation).

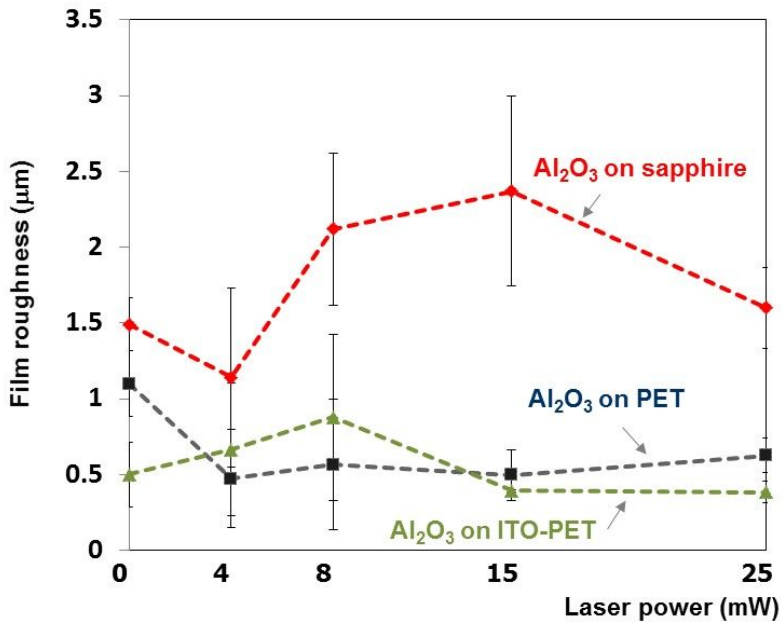


Figure 17 Film roughness of Al_2O_3 deposition on various substrate using direct laser method

The hardness and modulus on the depth of 10% of film thickness without laser were 6.93MPa, and 1.72GPa, respectively, and the results with 4mW laser were 24.3MPa, and 5.13GPa, respectively. The hardness and modulus were increased with laser assistance.

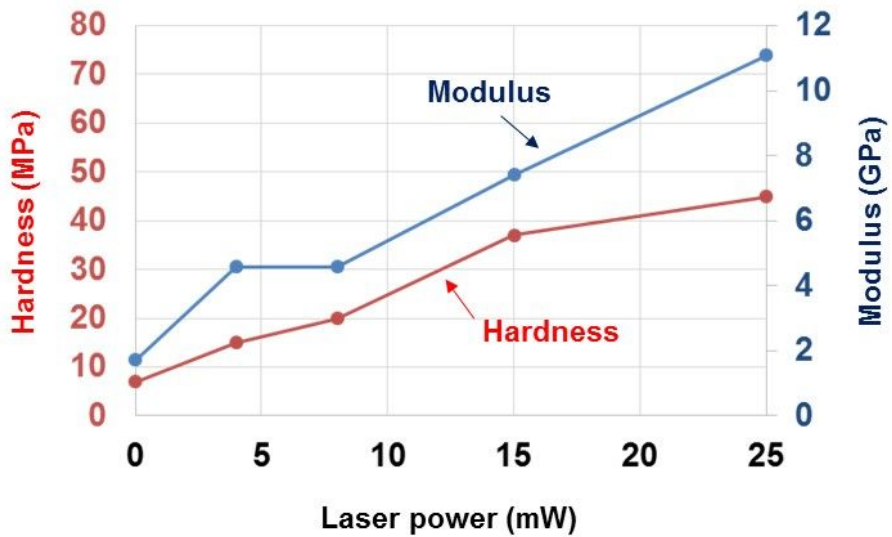


Figure 18 Mechanical properties of Al₂O₃ deposition results - Direct laser method

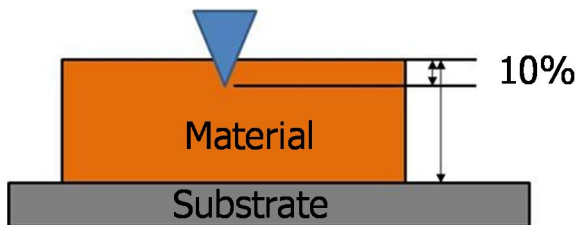


Figure 19 Schematic diagram of nano indentation method

In order to check phase transformation of Al_2O_3 film by laser beam, X-ray diffraction (XRD) was observed. XRD patterns revealed the peaks for polycrystalline $\alpha\text{-Al}_2\text{O}_3$ and the peaks of substrates including a single crystallization peak for the (0 0 0 1) plane of sapphire substrate. The deposition results showed the similar diffraction peaks regardless of laser power as shown in Figure 14. However, additional diffraction peaks at 2θ near 31° and 33° were observed in Al_2O_3 film on sapphire substrate as shown in the dashed box of Figure 14. The peaks can be seen only in $\theta\text{-Al}_2\text{O}_3$. In the previous findings, the same peaks were observed in the Al_2O_3 film on the sapphire fabricated by NPDS without the laser, and the maximum temperature derived by impact analysis was reported as about 960°C between two particles. The $\theta\text{-Al}_2\text{O}_3$ can be obtained after sintering from 800°C to around 1000°C , and the $\alpha\text{-Al}_2\text{O}_3$ can be obtained after sintering at higher than 1200°C [19]. In the deposited Al_2O_3 film without laser use, the peaks of $\theta\text{-Al}_2\text{O}_3$ were absent after 1200°C sintering. Similarly, the $\theta\text{-Al}_2\text{O}_3$ peaks decreased as the laser power increased in this study, so the laser could increase the maximum temperature and the $\theta\text{-Al}_2\text{O}_3$ could be transformed to $\alpha\text{-Al}_2\text{O}_3$.

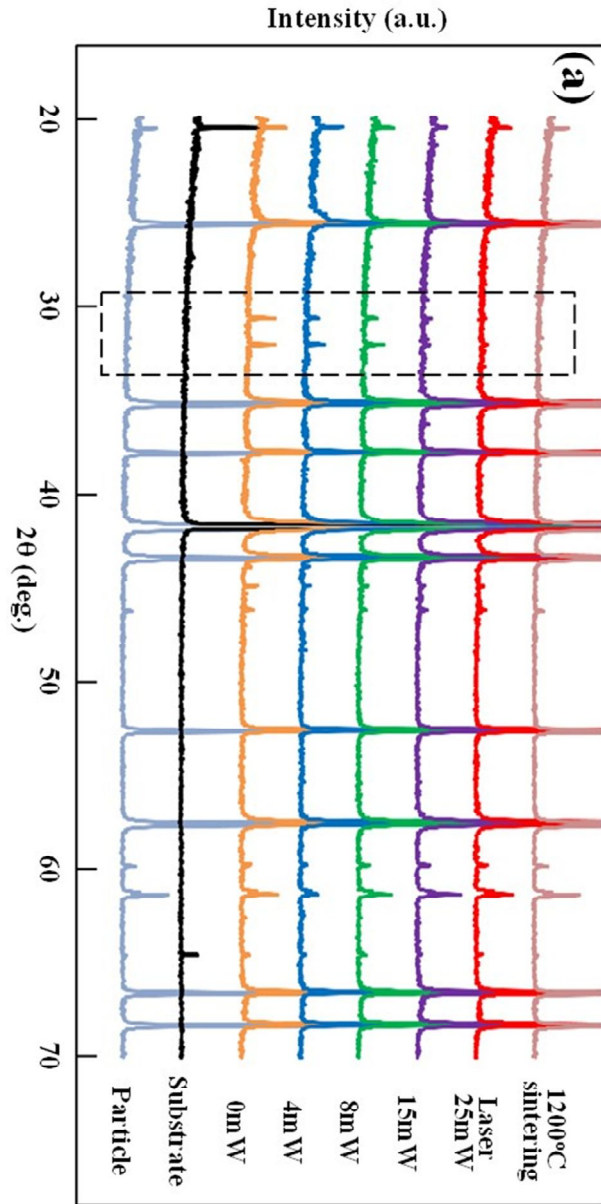


Figure 20 XRD results of Al_2O_3 deposition results - Direct laser method

3.3. TiO₂ particle deposition

Titanium dioxide has been used for many years in a various field of industrial and consumer goods including paints, coatings, adhesives, catalyst systems. TiO₂ is thermally stable, non-flammable, and poor soluble. Generally it is sourced from ilmenite, rutile and anatase. In this paper TiO₂ nanoparticles (15 nm, Nanoamor, USA), figure 21, was deposited onto ITO-PET via LaNPDS.

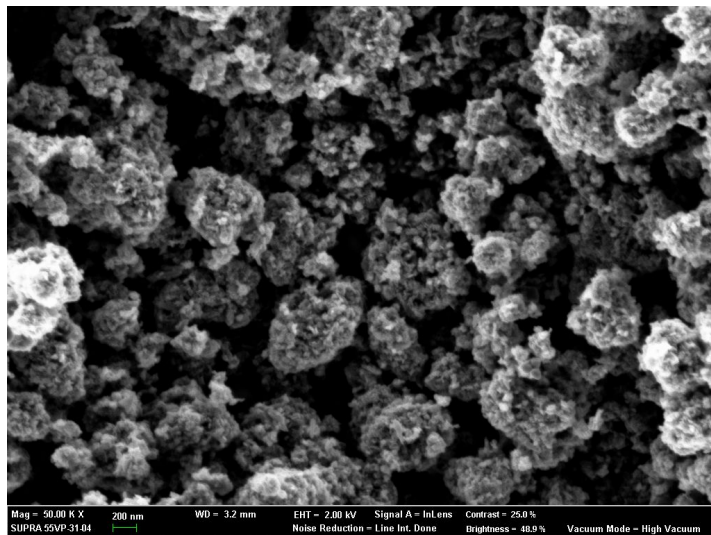


Figure 21 SEM image of TiO₂ particle

3.3.1. Direct laser method results

The mechanism of direct LaNPDS is as follows;(1) the impurities (water/oil) in the compressed air were removed, (2) the filtered compressed air mixed with raw TiO₂powders without solvent material in an aerosol generator (The Fluidized Bed Aerosol Generator 3400A, TSI), was used and (3) the nanoparticle–air mixture flowed into nozzle and deposited on the substrate by high kinetic energy in low vacuum condition. An ultraviolet (UV) laser beam with its wavelength of 355 nm was simultaneously induced on TiO₂ layer during deposition.

The laser power intensity was varied from 0 to 25 mW to minimize damage of substrate and to find condition for proper particle necking. And the power of laser was measured on the entrance of nozzle using the laser power meter.

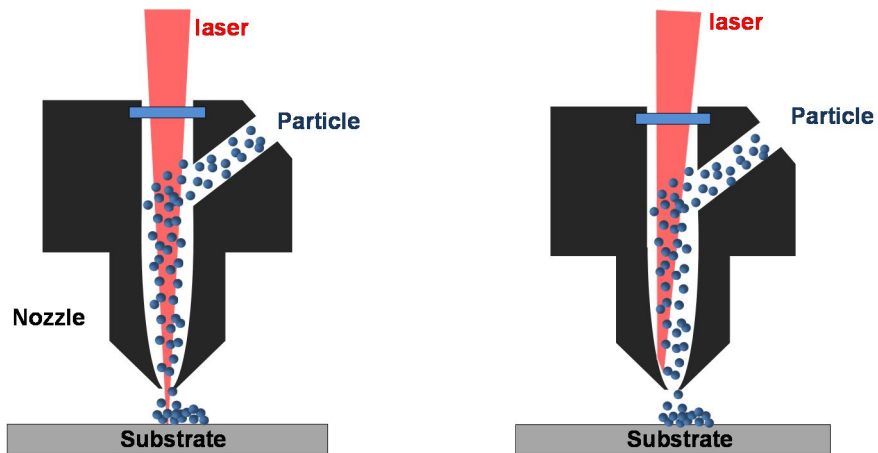


Figure 22 The pros and cons of direct laser method

- Flying particle energized by laser (coaxial with particle flow direction)
- Local sintering effect on the substrate
- **Damage occurred on substrate**
- Flying particle energized by laser
- **Unavailable to control laser reflection**
- **Difficult to know about laser dose rate**

At the figure 22, it is the SEM results of top surface and cross section of deposited TiO_2 particles. When deposit the TiO_2 using LaNPDS the surface morphology was more dense and compacted. For a more quantitative measurement, do the Braun Auer Emmett Teller (BET) test. Normally paste type fabrication method show $60 \sim 70 \text{ m}^2/\text{g}$ but in case of without laser condition shows $31 \text{ m}^2/\text{g}$ and in the LaNPDS case shows $94 \text{ m}^2/\text{g}$. As a result of surface morphology of SEM image, laser assisted condition get the more large surface area.

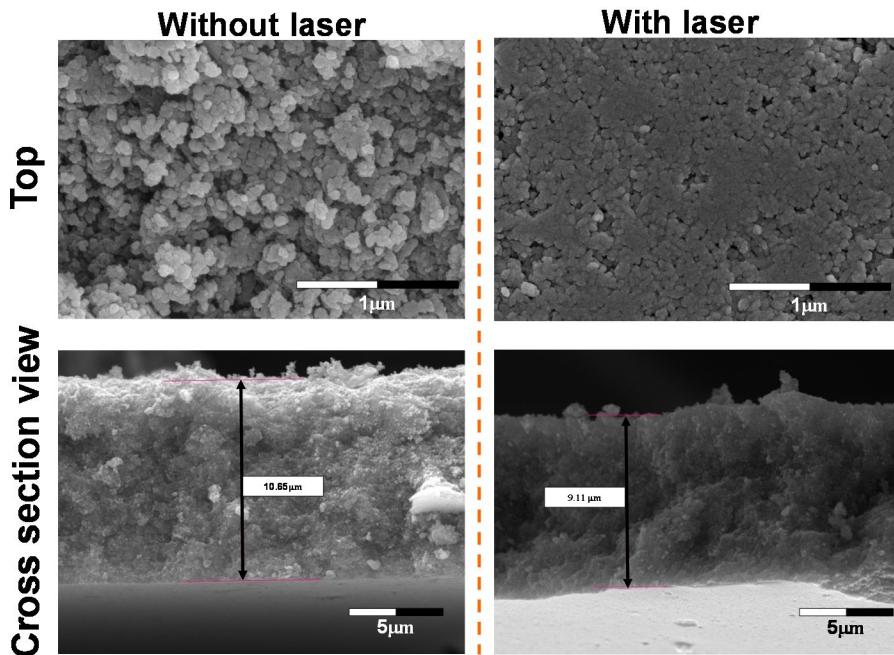


Figure 23 SEM image of TiO_2 deposition result by direct laser method

Same as the Al_2O_3 particle, after deposit the TiO_2 material on the ITO-PET substrate, thickness and hardness were measured by Dektak 6M surface profiler (Veeco Instruments, Tucson, AZ, USA) and nanoindentation (MTS XP, MTS System Corporation). Nano indenter result at figure 16. And hardness increased form 0.226 GPa to 0.317GPa. Also elasticity modulus increased from 1.703 GPa to 5.134 GPa.

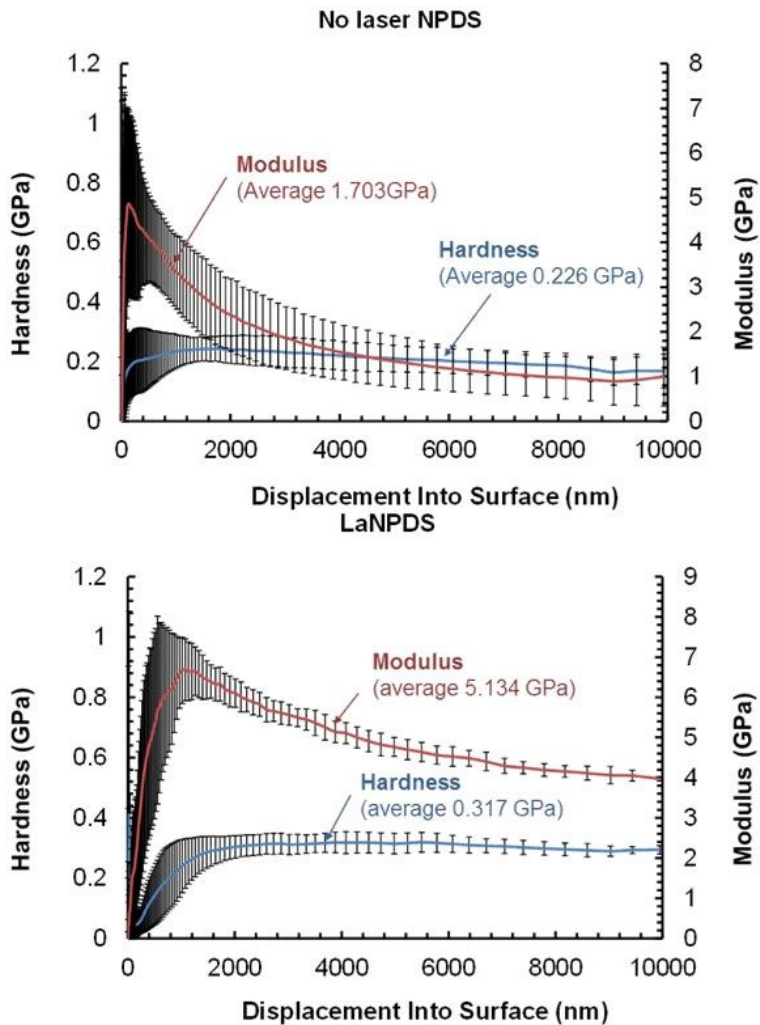


Figure 24 Mechanical properties of TiO_2 deposition result

3.3.2. In-direct laser method results

The surface morphology of In-direct laser method results is similar to the direct laser method. When apply the laser during the deposition process, the surface morphology became smooth. Figure 24 shows result of deposited TiO_2 film by LaNPDS (In-direct method). Without laser condition there are many small particles on the surface of deposition result. Depending on the intensity of the laser increased small particles were removed.

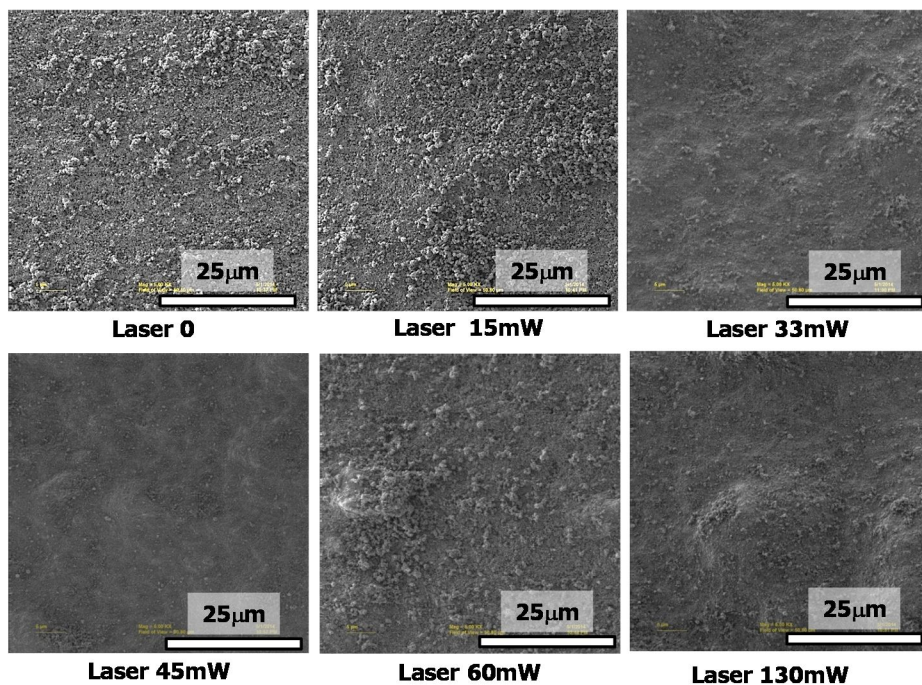


Figure 25 SEM image of deposited TiO_2 surface morphology

Figure 25 shows SIM image of deposited TiO₂ cross sections, fabricated by FIB milling process. And figure 26 is results of TiO₂ film thickness. When apply the laser during the deposition. The deposition thickness was thinned in accordance with the power of the laser increased. But the porosity show the opposite trend. When apply the laser, the density of the cross section image seems high. In order to determine the hardness, indentation test was performed. Figure 27 shows hardness results. As expected, with the laser condition result had a high value of hardness.

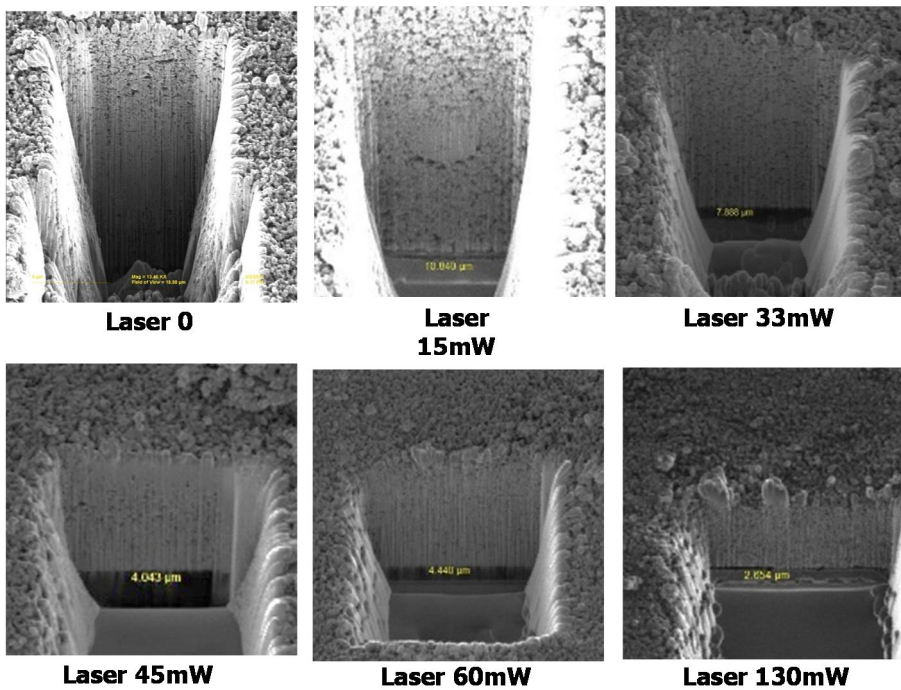


Figure 26 SIM image of cross section of TiO₂ film fabricate by FIB milling

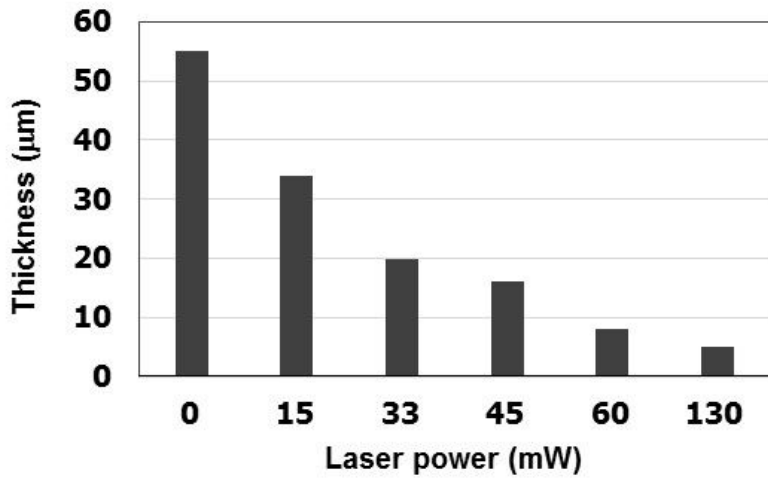


Figure 27 Thickness result of deposited TiO₂ particle

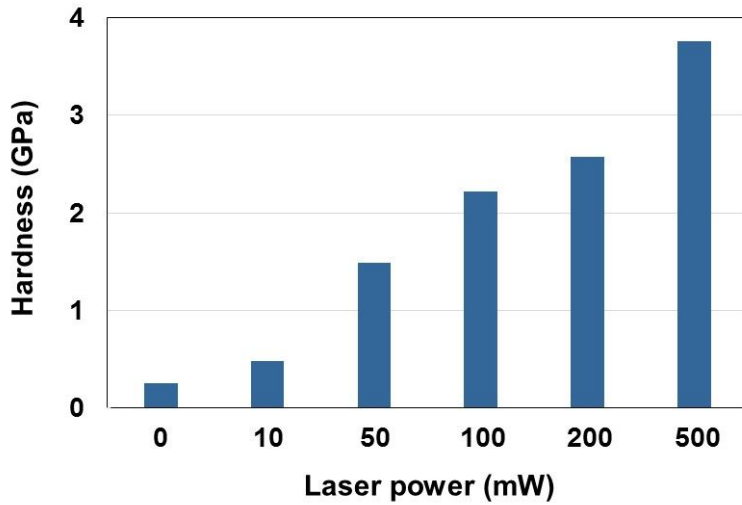


Figure 28 Indentation result of deposited TiO₂

Chapter 4 Effect of laser on flying particle

4.1. Overview

Experimental results using the LaNPDS, mechanical properties of bonding was increased observed in ceramic (Al_2O_3 , TiO_2) materials. Instinctively, laser power transfer to flying particle. This process is based on the interaction of a pulsed laser with nanoparticles. The pulsed laser irradiation can utilized for thin film melting, patterning, and printings [20, 21, 22].

In order to explain the phenomena that occur inside the tube should be noted further information about flying particle and compressed air medium conditions. To solve this problem experiment set-up suggested like in figure 28. Prepare the 300 mm length stainless steel pipe (ANSI Sch40), and the pipe inner diameter is 8 mm.

Pressure gauge and thermos couple were installed, and micro-particle image velocimetry (micro-PIV) was suggested. PIV measurement results confirmed by commercial analysis software ANSYS. Particle path geometry modeled.

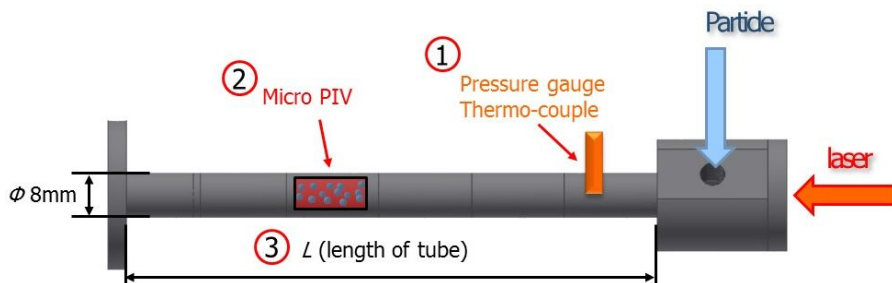


Figure 29 Schematic diagram of laser and particle mixed tube

4.2. Evaluation of laser effect on flying particle

In order to evaluate the influence of the laser for flying particle. For the capturing of flying particle at the end of tube, install the mesh grid as much as possible not to interrupt the compressed air and particle flow. Figure 29 shows installed mesh grid.

Sapphire wafer attached on the mesh grid to compare the deposition results through the nozzle condition. From 0 W to 2 W laser power conditions were used. Figure 30 shows captured flying particle results. The adhesion strength was poor between Al_2O_3 particle and sapphire wafer.

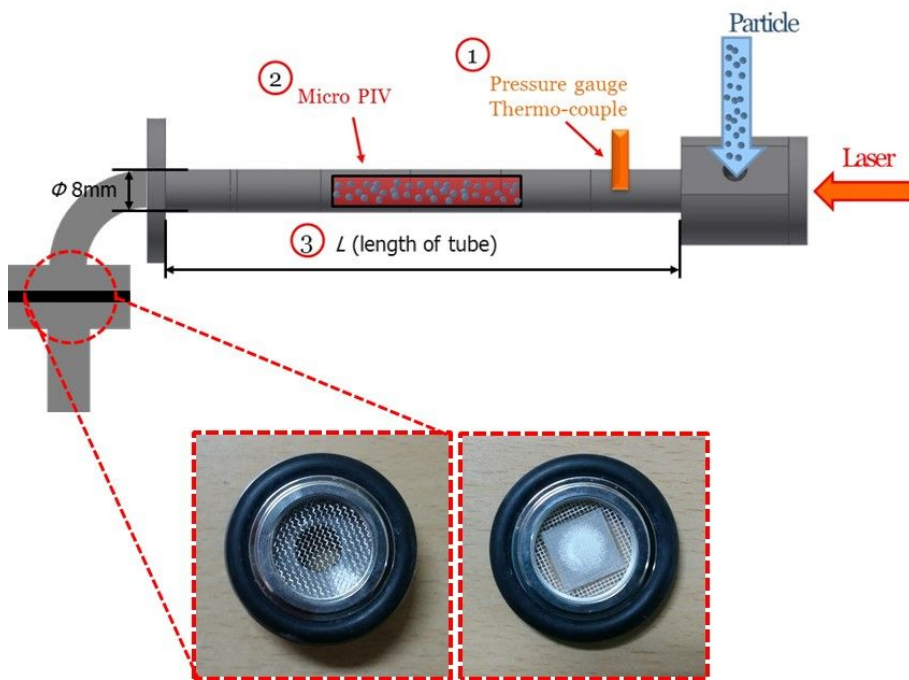


Figure 30 Schematic diagram of flying particle capturing experiment set up

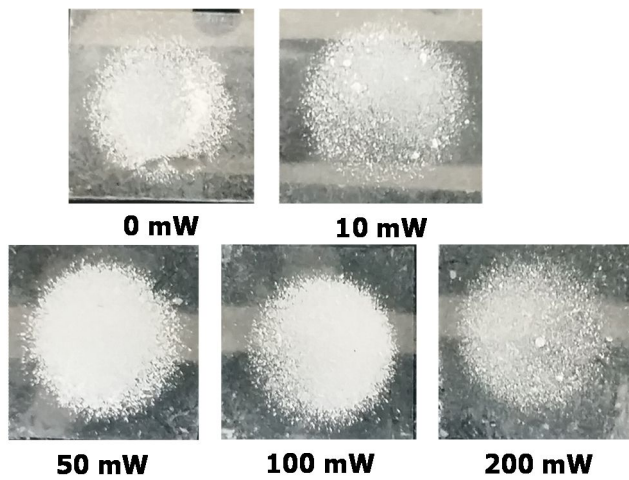
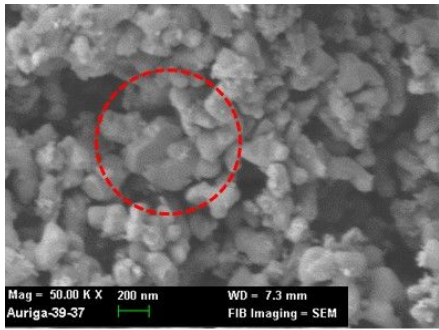
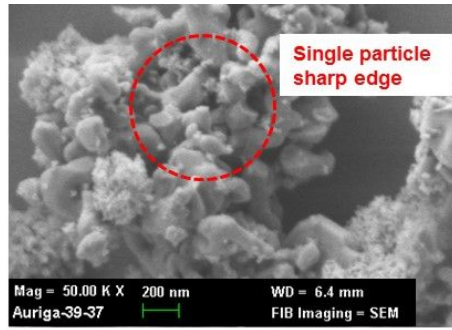


Figure 31 Figure of inner mesh and captured Al₂O₃ results

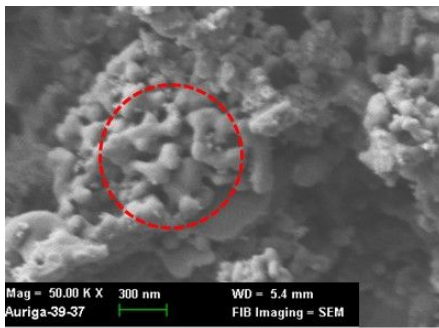
Figure 31 show FE-SEM image of captured Al₂O₃ particle. Depending on the intensity of the laser, the shape of particle edge was changed. In without laser condition there are sharp edges exist. But in the laser conditions the edge shape became rounded and the morphologies of the particles were similar to the sintering and necking phenomena. And particles seems to have increased more and more lumped.



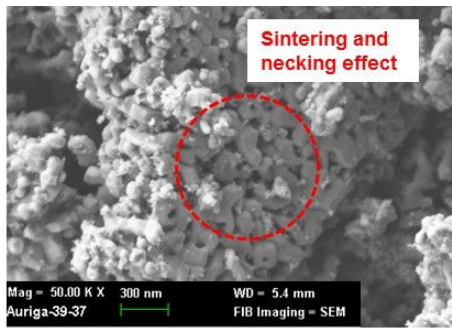
Al₂O₃ particle



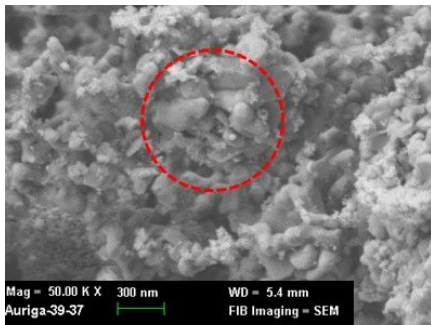
0 mW



10 mW



50 mW



200 mW

Figure 32 FE-SEM image of captured flying Al₂O₃ particle

Same as the earlier evaluation, in order to check phase transformation of Al_2O_3 film by laser beam, X-ray diffraction (XRD) was observed. Polycrystalline $\alpha\text{-Al}_2\text{O}_3$ and the peaks of substrates including a single crystallization peak for the (0 0 0 1) plane of sapphire substrate were detected. The particle capturing results showed the similar diffraction peaks of deposition result using nozzle.

In the figure 32, there were diffraction peaks at 2θ near 31° and 33° , $\theta\text{-Al}_2\text{O}_3$ phase were observed in captured Al_2O_3 particles on sapphire wafer without laser condition. As with the previous results in laser assist condition $\theta\text{-Al}_2\text{O}_3$ peaks were removed. This results means particles were excited by laser during the flight and make a sintering effect. And also have a phase change $\theta\text{-Al}_2\text{O}_3$ to $\alpha\text{-Al}_2\text{O}_3$ after particle impact on the substrate. The phase change start from 40 mW laser power and more powerful conditions (< 2 W) shows same results.

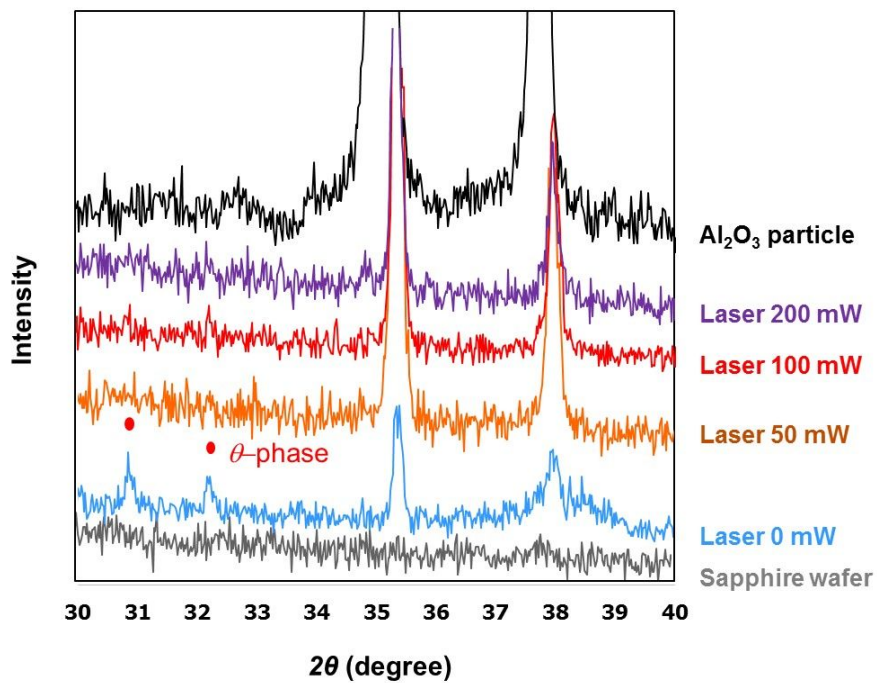


Figure 33 XRD measurement results of captured flying Al₂O₃ particle

4.3. Particle velocity measurement

Methods for in-line particle measurement in a dispersed two-phase flow mainly include the optical, ultrasonic, and electric methods. The laser-based particle size analyzer is widely used in particle size measurement (Black, McQuay & Bonin, 1996) [23], but is rarely used to measure the particle velocity and spatial distribution of particle concentration (Inaba & Matsumoto, 1999) [24]. In addition, determination of the particle refractive index is still a difficult problem (Kinoshita, 2001) [25], and the laser-based particle size analyzer is not optimized to measure the two-phase flow at very low particle concentrations. The phase Doppler particle analyzer (PDPA) (Doudou, 2005; Du, Yao, & Lin, 2005; Han, Wang, & Ma, 2010; van den Moortel, Azario, Santini, & Tadriss, 1998) [26-29] can simultaneously measure particle size, velocity, and concentration, but its pointwise measurement method makes an assumption of spherical particles, which is not always true in actual processes. Particle image velocimetry (PIV) (Kumara, Elseth, Halvorsen, & Melaaen, 2010) [30] is a flow-field visualization technology that permits measurement of the instantaneous velocity and its related properties in fluids seeded with tracer particles, but does not provide any information about the concentration and size of the actual particles (Kashyap, Chalermssinsuwan, & Gidaspow, 2011) [31]. In the last few years, ultrasonic attenuation spectroscopy (UAS) and focused beam reflectance measurements (FBRM) have emerged in industrial applications for measuring the concentration and particle size distribution (PSD) in dense two-phase flows (Sarkar, Doan, Ying, & Srinivasan, 2009) [32]. In addition, the particle concentration in terms of the particle volume fraction has been measured using a microchannel with 12 multi-layered electrodes, which bases its measurements on the cross-sectional capacitances of the micro particles in the flow (Othman et al., 2013) [33]. To our knowledge, however, there is no in-line and in situ measurement

technique that can simultaneously measure the size, velocity, and concentration of particles in an extremely diluted two-phase flow.

It is well known that image-based methods offer the potential to extract both qualitative and quantitative PSD information based on direct visualization of the process. Image processing also provides a deeper understanding of the process by providing more realistic and credible two-dimensional information on the particle shape and size [34].

4.3.1. Hardware set up of micro PIV system

In this research, measurement system was proposed a method based on trajectory image analysis for the in situ and in-line measurement of particle size, velocity, and concentration in dilute particulate two-phase flow. The measurement system consists of a common industrial CCD camera, a halogen lamp and long working distant lens. And for the image processing use the commercial software.

The particle trajectory measurement system, as shown in figure 33. The digital CCD camera locate front of the transparent box. The tube fabricated modular type. Each basic element length is 25 mm the inner circle diameter in 8 mm. To measure the particle trajectory, middle of the tube module changed rectangular shape part, has inner size width: 8 mm and height: 8 mm, same as tube diameter. This part has the transparent window each side front and back.

Halogen lamp located at the back side of the box. For this work CCD camera with a frame exposure mod to ensure that capture images of flying particles as particle traces. The resolution of the camera was 1024 pixels \times 1024 pixels and exposure time was 5 μ s. The positions of measured particles are random in the viewing field depth, lens had 20 mm working distance. For capture the image from the center of tube, in this research used $\times 50$ magnitude lens and the hardware set up as shown in figure 34.

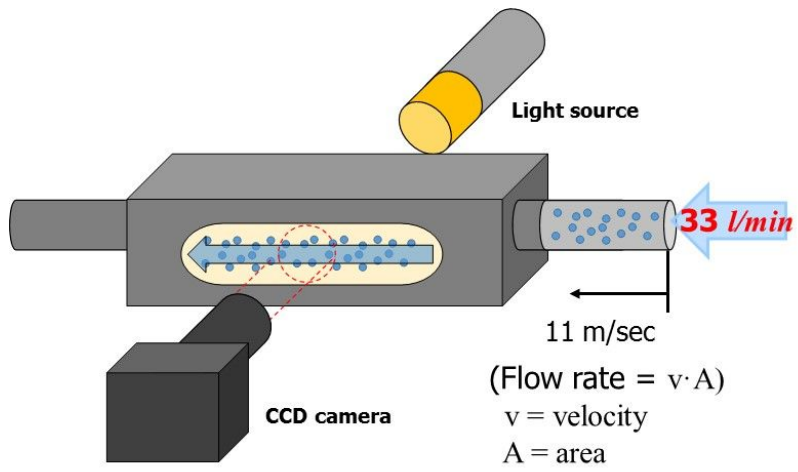


Figure 34 Hardware set up of PIV system

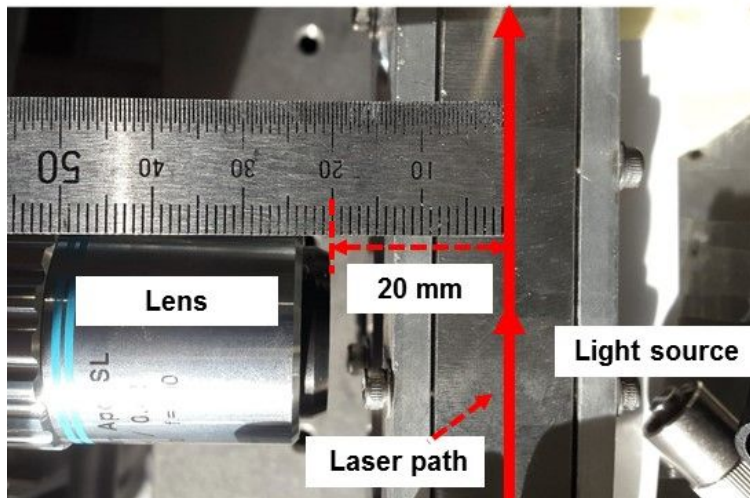


Figure 35 Figure of micro PIV system

Figure 35 shows flying particle highlighted by UV laser. 355 nm wavelength laser has blue light. The laser and tube were located coaxially, the direction of laser in left to right. At the figure 35 (A) there are no particles inside the box only laser go through the box. So the color was dimly. In contrast at the figure 35 (B) the blue color is brighter than (A). Because of at the (B) there were laser and flying particles exist coaxially. Laser was reflected at the flying particle, come out more bright light.

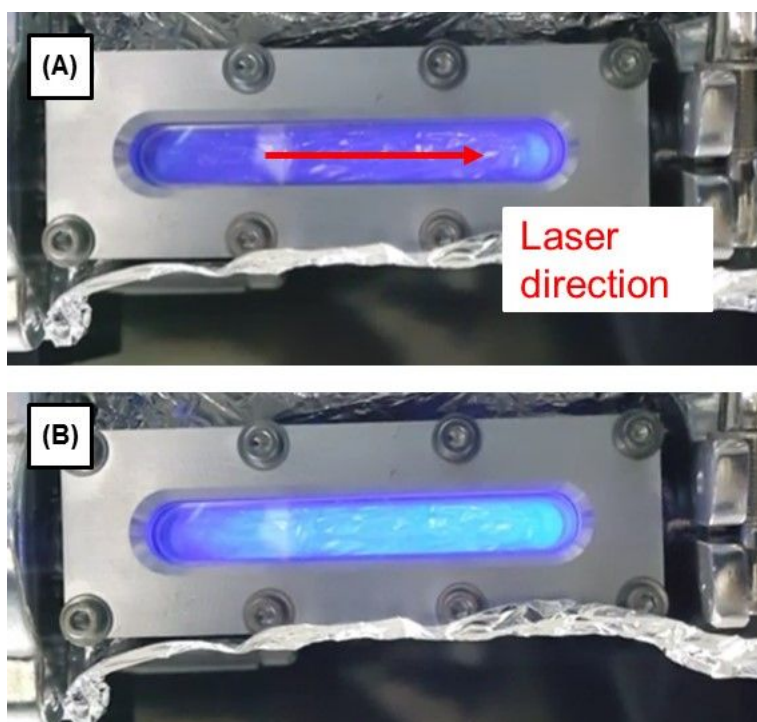


Figure 36 Figure of transparent window for flying particle observation (A) only laser turn on condition, (B) laser turn on with flying particle

4.3.2. Measurement of Zn particle velocity

Particle measurement system used Zn particle figure 36, has 10 ~ 20 μm size. Zn particle had spherical shape. If we use a smaller particle such as TiO_2 , Al_2O_3 , it is difficult to measurement with lack of resolution and brightness.

After chose the flying particle than check the resolution and calibrated. Figure 37 shows calibration process for accuracy.

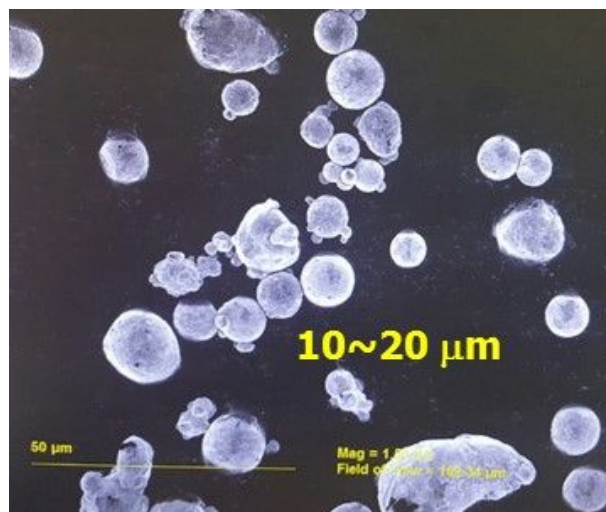


Figure 37 SIM image of Zn particle for PIV

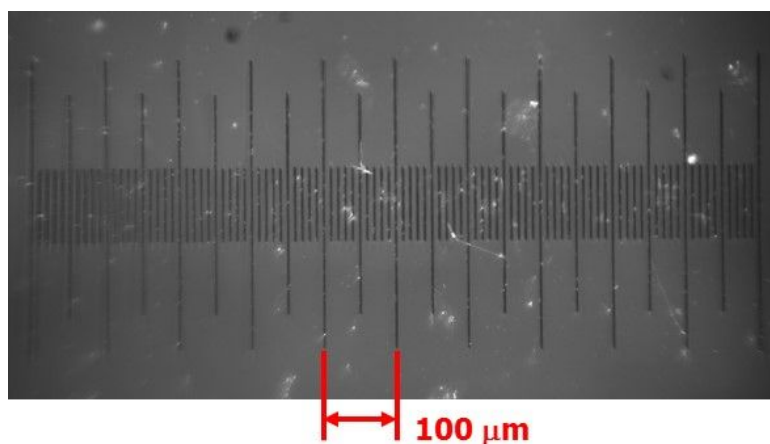


Figure 38 Referencing for size measurement

Figure 38 A, B, C shows particle trajectory capturing and image process. If the exposure time is not short enough, the result image of the flying particle will be shown as a trace of the particle motion. Figure 38 (C) shows the length, l , and width, d , of the trace, which are related to the velocity and the diameter of the moving particle, respectively. This research assumed particle diameter is D . by controlling the exposure time within a certain value t , the velocity V , and diameter D of the moving particle may be simply calculated as follow.

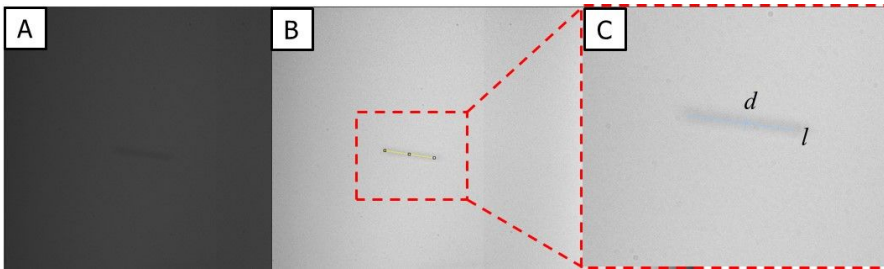


Figure 39 Particle size and velocity measurement

$$V = \frac{l}{t} \quad (1)$$

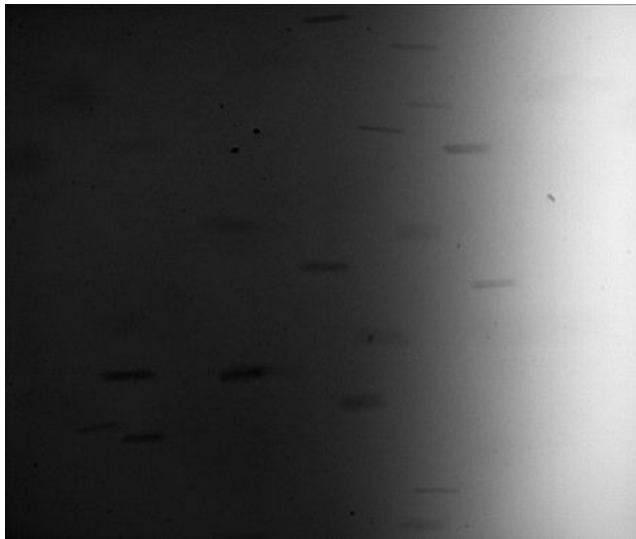


Figure 40 Captured Zn flying particle in 5 μsec

Figure 39 shows captured Zn flying particles. And figure 40 and 41 is calculated velocity of particles. Depending on the presence or absence of a laser, each case count 50 particles, than average the measured velocity and particle diameter.

In case of absence of a laser, the average particle size is 10.11 μm and the average velocity is 16.64 m/sec. In contrast, presence of a laser, the average particle size is 9.77 μm and the average velocity is 15.62 m/sec. Particle size and velocity of each case slightly different but in the same order. It is difficult define as the laser does not affect the speed of the particle.

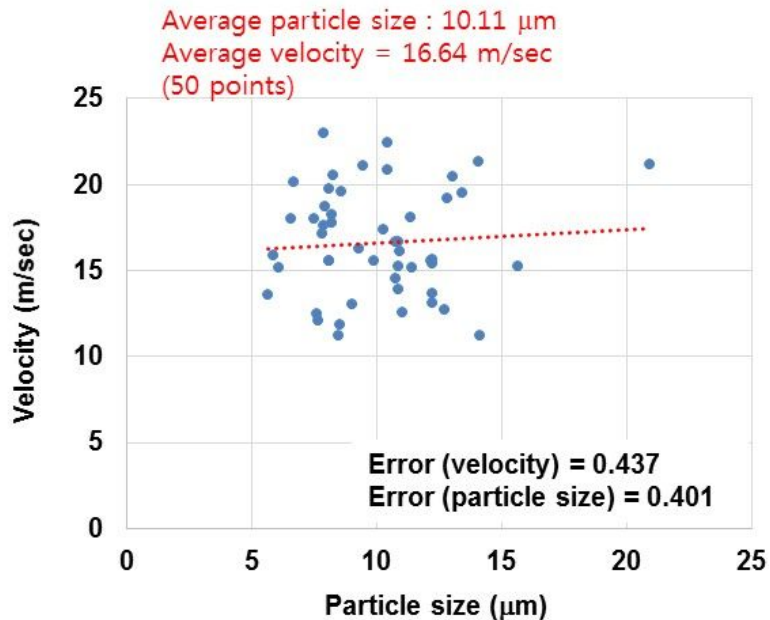


Figure 41 Zn particle velocity result - no laser power

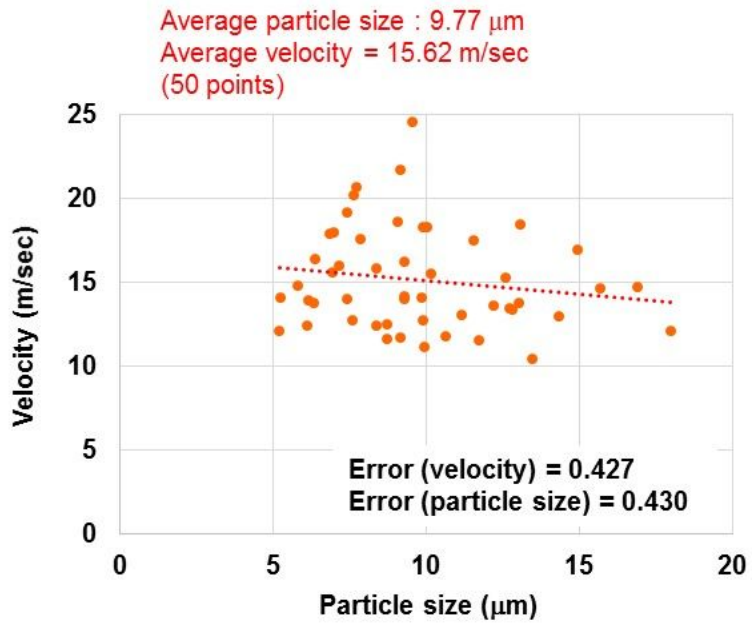


Figure 42 Zn particle velocity result - laser power 500 mW

4.4. Computational fluid dynamics

For the Computational fluid dynamics analysis, the commercially available ANSYS CFX was utilized. ANSYS CFX enables engineers and researchers to perform fluid-flow analysis of incompressible and compressible fluid flow and heat transfer in complex geometries. Also, they can import meshes, specify the materials, boundary conditions, and solution parameters, solve the calculations, view the results, then create reports using built-in tools [35].

The set of equations solved by CFX are the unsteady Navier-Stokes equations in their conservation form. The governing equations are the continuity equation, the momentum equation, and the total energy equation can be written as follows Equation (2)-(4) respectively.

$$\frac{\partial \rho}{\partial t} = -\rho \nabla \cdot U \quad (2)$$

$$\frac{\partial(\rho U)}{\partial t} + \nabla \cdot (\rho U \otimes U) = -\nabla p + \nabla \cdot \tau + S_M \quad (3)$$

$$\frac{\partial(\rho h_{tot})}{\partial t} - \frac{\partial p}{\partial t} + \nabla \cdot (\rho U h_{tot}) = \nabla \cdot (\lambda \nabla T) + \nabla \cdot (U \cdot \tau) + U \cdot S_M + S_E \quad (4)$$

Where ρ is density, t is time, U is velocity vector, p is pressure, τ is stress tensor, S_M is the momentum source, h_{tot} is the total enthalpy, λ is thermal conductivity, and S_E is the energy source. In the momentum equation, the stress tensor τ is related to the strain rate expressed as equation (5)

$$\tau = \mu(\nabla U + (\nabla U)^T - \frac{2}{3} \delta \nabla \cdot U) \quad (5)$$

where δ is identity matrix. In the total energy equation, the total enthalpy h_{tot} is expressed as equation (6). The term $\nabla \cdot (\mathbf{U} \cdot \boldsymbol{\tau})$ represents the work due to viscous stresses, and the term $\mathbf{U} \cdot \mathbf{S}_M$ represents the work due to external momentum sources.

$$h_{tot} = h + \frac{1}{2}U^2 \quad (6)$$

Additionally, the ideal gas equation of state was used as expressed in equation (7)

$$\rho = \frac{wp}{R_o T} \quad (7)$$

where w is the molecular weight of the gas, and R_o is the universal gas constant.

The governing equations explained in the previous and the analysis conditions for CFD were summarized in table 4.

Table 4 CFD analysis condition

Class	Models	Condition
Flow	Energy model	Total energy with inviscid work
	Turbulence model	Shear Stress Transport (SST) model
Particle	Transport model	Lagrangian particle tracking
	Drag transfer	Schiller Naumann
	Heat transfer	Ranz Marshall
Boundary condition	Boundary velocity	No slip condition
	Heat transfer	Adiabatic
Inlet	Constraint	Pressure (Gas pressure), Temperature
Outlet	Constraint	Pressure (Vacuum), Temperature

4.4.1 CFD modeling

The modeling information is shown in the figure 42. The total length of flying particle and air tube is 300 mm and for the initial velocity of tube, previous compressed air flow 200 mm also modeled. Zn particle has molar mass = 65.38 g/mol, density = 7.14 g/cm³ and particle sized used 10 μm measured by PIV. Input air condition is mass flow rate = 0.68 g/s, temperature = room temperature (298 K) and for the flow set the initial velocity = 1 m/s. Outlet pressure was same as vacuum chamber conditions, pressure = 0.107 MPa and temperature = room temperature (298 K).

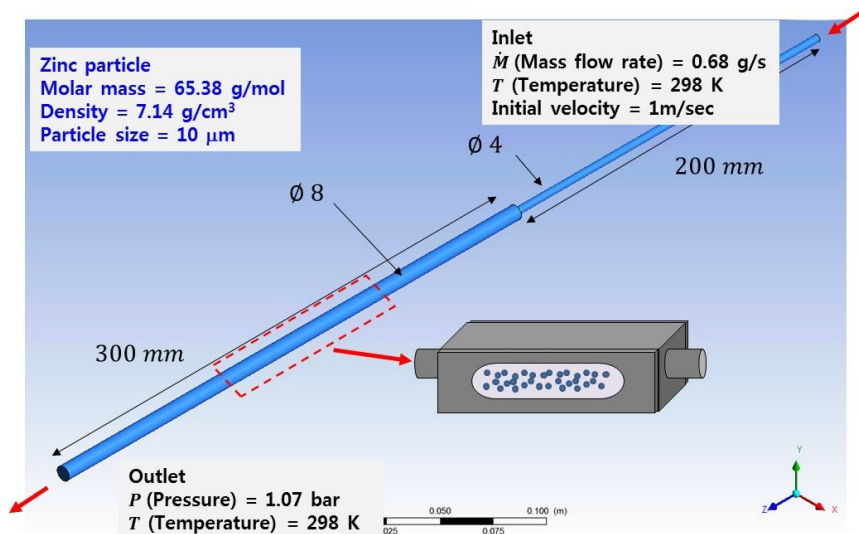


Figure 43 Geometry and boundary conditions for simulation

4.4.2. CFD analysis

The velocity of air shown as figure 43. The velocity increased inside the small tube from 1 m/s then entered laser and particle mixture tube about 48 m/s. After pass the B section, flow speed was slow down depending on the expansion of cross section area. In the middle point of the tube, air velocity is about 12.53 m/s.

And figure 44 shows velocity of Zn particle. It takes time for following the air flow for the inertia. But eventually particle velocity had similar speed with air flow. In the middle point of the tube, Zn particle velocity is 12.36 m/s.

Even if, there was a small difference in the micro PIV measurement and CFD analysis, analysis results could trust. After modeling the Zn particle then input the Al_2O_3 material properties, then calculated the velocity. In case of Al_2O_3 , the velocity is 12.59 m/s at the middle point. Table 5 shows the results of micro-PIV and CFD analysis.

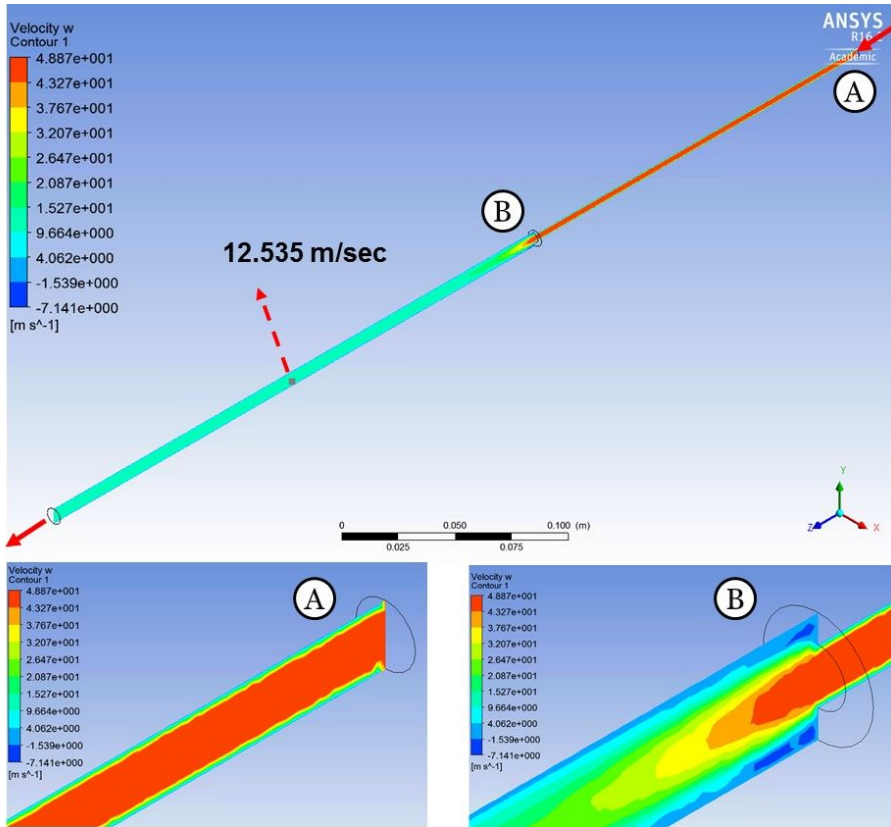


Figure 44 Air flow simulation result

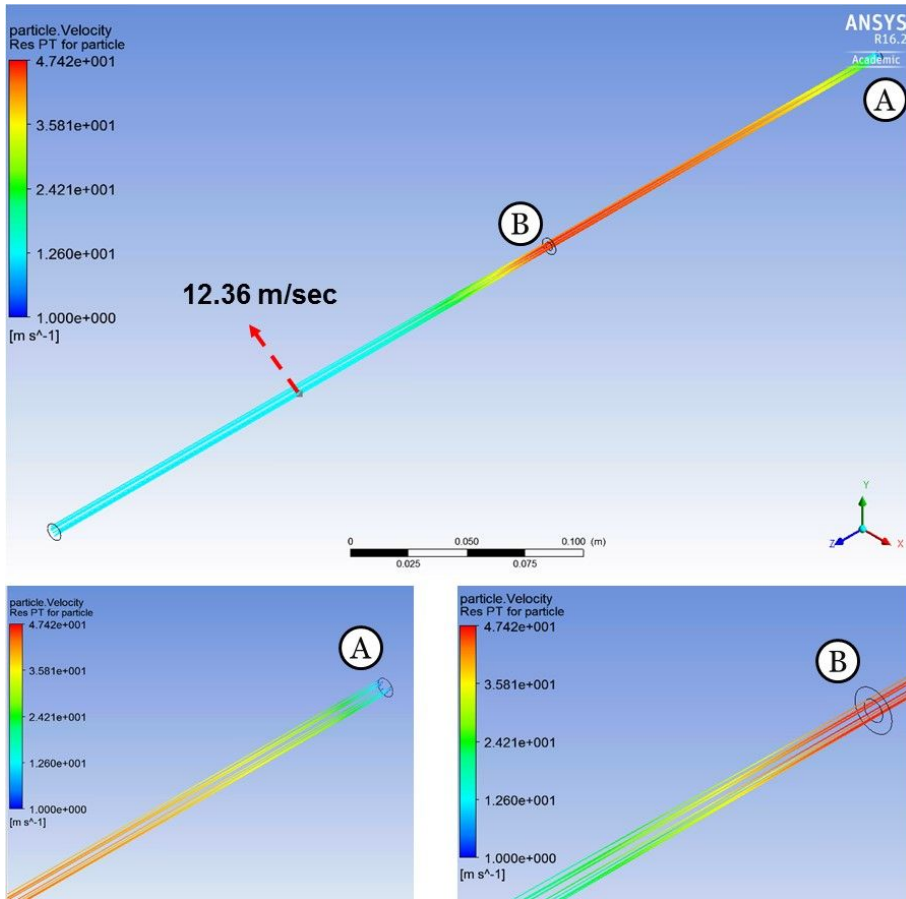


Figure 45 Particle velocity simulation result

Table 5 Results of simulation and PIV measurement

	Conditions	Velocity(m/sec)
PIV measurement	Without laser	16.64
	Laser 500 mw	15.62
Simulation	Air	12.54
	Al ₂ O ₃ particle (5 μm)	12.59

Chapter 5 Applications

5.1. Overview

A Dye Sensitized Solar Cell (DSSC), shown in Figure 3, was developed by O'Reagan and Grätzelin 1991 [36]. It involves the use of an n-type semiconductor oxide dye, electrolyte and transparent electrodes. Various semiconductor oxides such as TiO_2 , SnO_2 , ZnO and In_2O_3 have been studied as potential photoelectrodes of DSSC [37]. Here, TiO_2 shown in Figure 45 was used for as the photoelectrode because of its wide band gap, stability and low production cost as the key advantages.

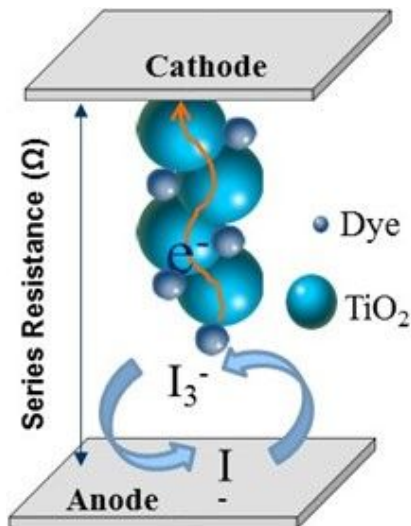


Figure 46 Schematic diagram of Dye Sensitized Solar Cell

5.2. Fabrication and evaluation of Dye Sensitized Solar Cell (DSSC) and Electro Chromic Window (ECW)

Compared to other solar cells, DSSC has the competitiveness in the fabrication process, cost, and convenience. DSSC has the advantages in portability and lightweight, it can be applied to electronics, transportation, defense industry, sports field. Since DSSC also has the better penetrability than solid type solar cell such as silicon based type, it can be used in interior part or building integrated photovoltaic (BIPV) parts. Especially, flexible DSSC, polymer based substrate, can be applied in a wide a range.

In the conventional DSSC fabrication process, semiconductor oxide paste should be coated on the working electrode, and sintered in the high temperature [38, 39]. Even though many researches were proposed to replace the high-sintering process, almost methods still have been used the paste or solution type's semiconductor oxide, and required the additional equipment, chemical method, or pre-treatment process such as microwave, UV irradiation, and hydrochloric acid (HCl) treatment, etc.

In the study, the semiconductor oxide layer of TiO_2 was fabricated on two different types of electrodes namely glass and a polymer substrates via LaNPDS in order to evaluate whether the method can be used to successively fabricate the flexible DSSC and improve efficiency. To assess these two issues, TiO_2 was deposited on both glass and polymer substrates of 15 ohms/square indium tin oxide coated polyethylene terephthalate (ITO-PET) with or without laser assistance.

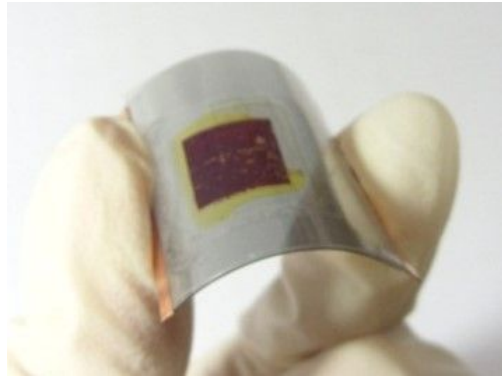


Figure 47 Flexible DSSC fabricated by LaNPDS

The efficiency of fabricated DSSCs were obtained by solar simulator (K201-LAB 50, Polaronix); it adopted a xenon lamp and the light illumination intensity of 100 mW/cm^2 (AM 1.5) under atmospheric conditions.

Figure 46 shows flexible DSSC fabricated by LaNPDS. Since this is a room temperature deposition process, we can coat any type of nanoparticles onto flexible substrates such as indium tin oxide-polyethylene terephthalate (ITO-PET). Conventionally, thermal sintering process at $500 \text{ }^\circ\text{C}$ after forming TiO_2 layer is required for necking among adjacent particles. However, flexible substrates can withstand temperature only up to $150 \text{ }^\circ\text{C}$. Therefore, it is difficult to form TiO_2 photo-electrode on flexible substrates with its existing thermal sintering process. To overcome this problem, La-NPDS was designed and used to minimize damage on a flexible substrate during sintering and to induce its necking among adjacent TiO_2 nanoparticles.

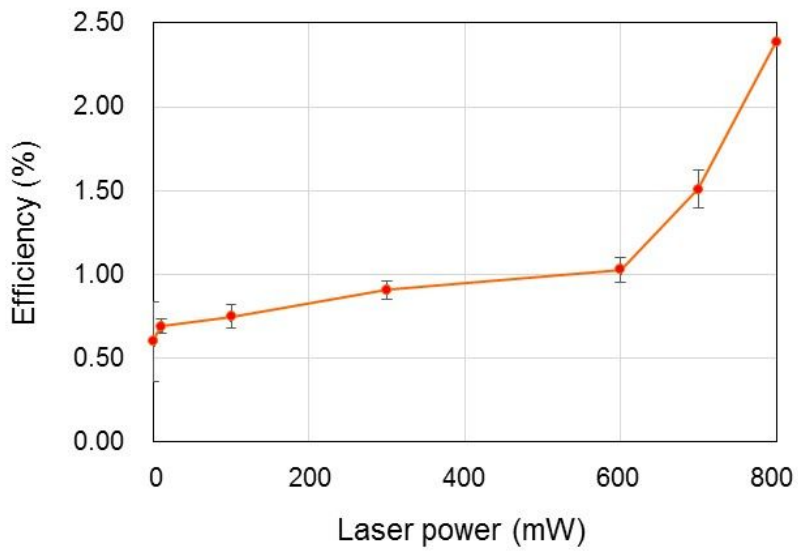


Figure 48 DSSC efficiency result - In-direct laser method

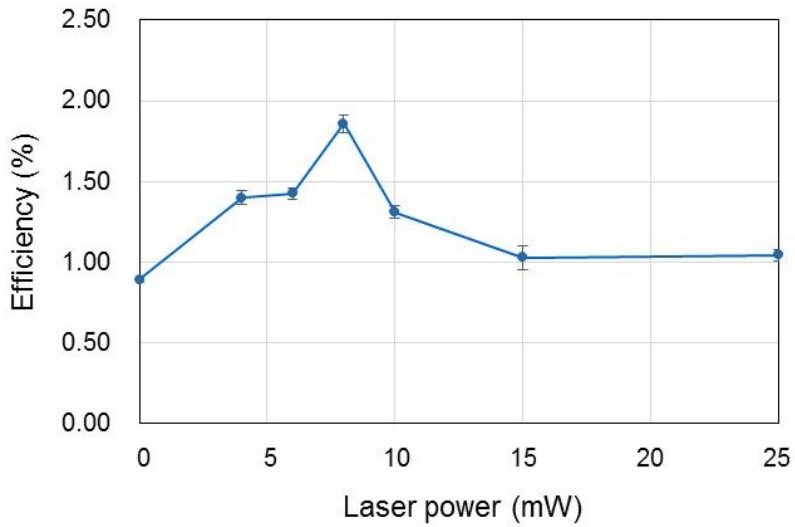
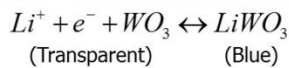
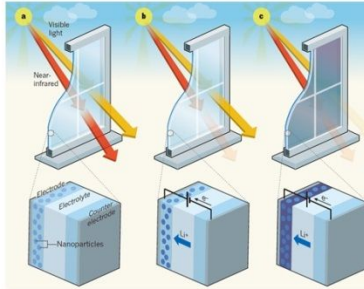


Figure 49 DSSC efficiency result - Direct laser method



Electrochromic Window

Ref) BRIAN A. KORGEL, "Composite for smarter windows", MATERIALS SCIENCE, NATURE, VOL 500, 15 AUGUST 2013.



Scheme of Electrochromic Window

Figure 50 Background of ECW

The NPDS technique enables the deposition of metal and ceramic particles with sizes from 10 nm to 100 μm on substrates including ceramics, metals, polymers, and papers, without requiring precursors. It is a relatively simple and low-cost method of film deposition. It is even suitable for the mass production of thin films in electrochromic window fabrication, which has received much recent research attention. Here, we demonstrate the fabrication of WO_3 films for EC device applications by using NPDS [40]. And also using the LaNPDS process, increasing the different of transmittance.

Follows are definitions about ECW.

- Electrochromism : reversible change in a material's optical properties (transmittance, absorbance and reflectance) under an applied voltage
- Electrochromic materials : many transition metal oxide materials, some organic molecules and polymers
- Electrochromic Window (ECW) : a dynamic windows allowing us to control daylight, solar heat gain, and internal heat loss through windows of buildings and vehicles

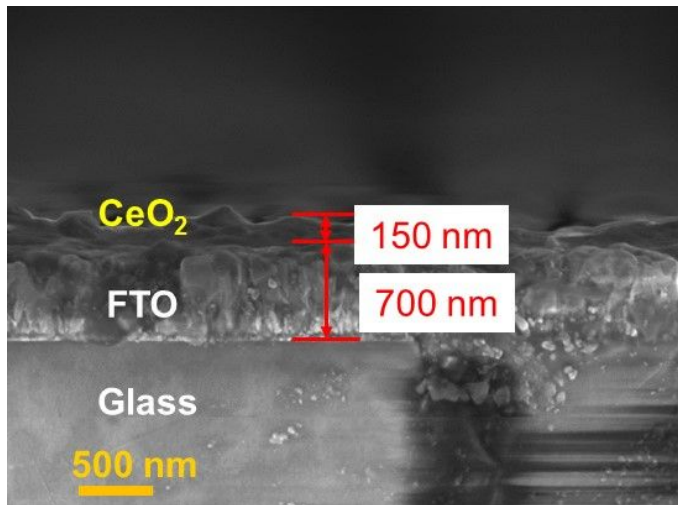


Figure 51 FE-SEM image of cross section of the CeO₂ film on FTO glass

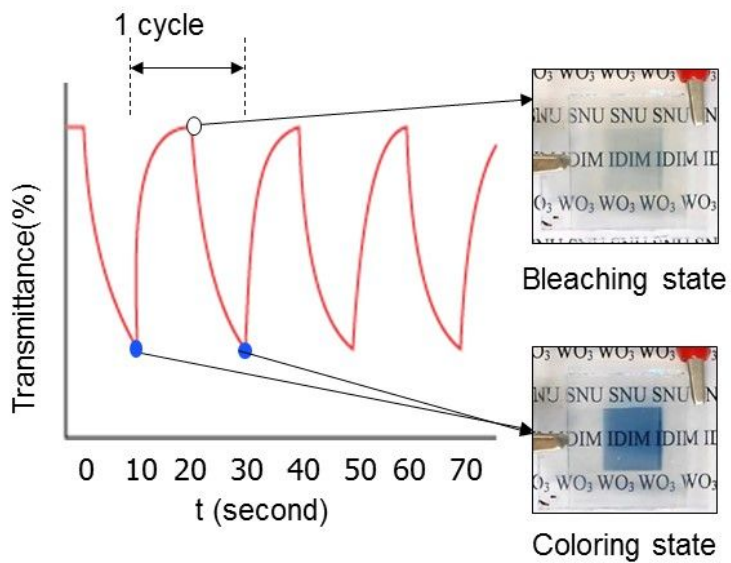


Figure 52 Applied voltage change and transmittance change over cycle test

As Figure 50 WO_3 particles were deposited on the FTO-glass substrate. The thickness of CeO_2 film was about 150 nm. ECW was successfully fabricated as Figure 51. And repeatedly evaluate the coloring and bleaching test.

Figure 52 shows transmittance result of ECW fabricated by without laser condition. In bleaching condition the transmittance was 55% and the difference of transmittance between bleaching and coloring was 13.8% at an 800 nm wavelength. To improve the change of transmittance LaNPDS was used, Figure 52 shows the result. In this time the maximum transmittance change was 16%.

This result shows when deposit the WO_3 particle using LaNPDS, the connection between each particles was improved by sintering and necking phenomena caused laser effect.

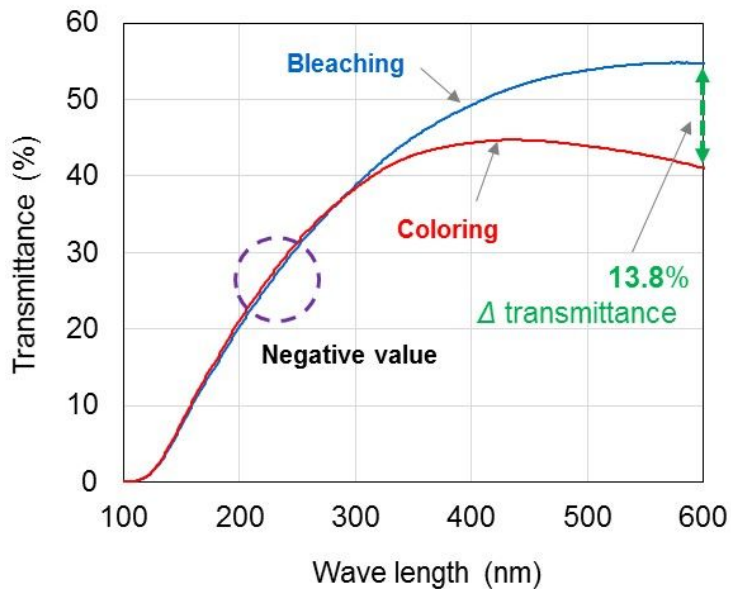


Figure 53 Transmittance result of without laser condition (in-direct laser method)

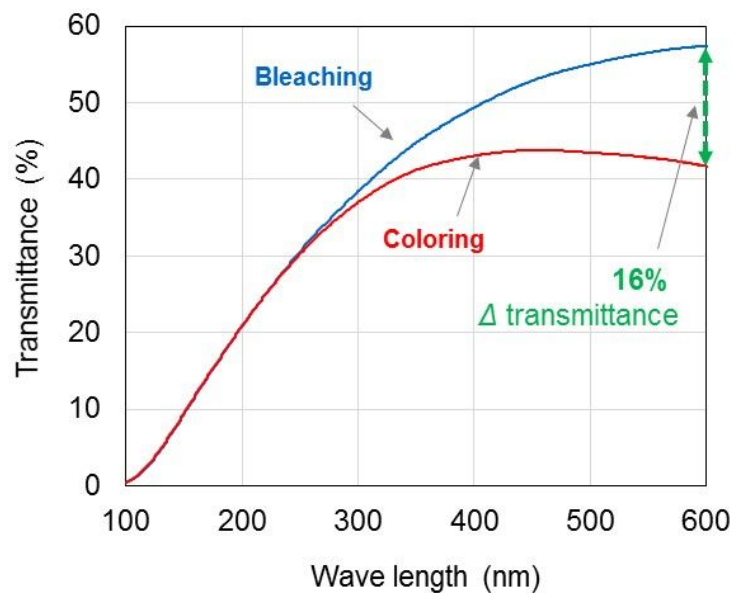


Figure 54 Transmittance result of with laser condition (in-direct laser method)

Chapter 6 Bonding mechanism

6.1. Overview

Laser cladding and a solid-state sintering mechanism are the main theories in the phenomenon of LaNPDS. In this chapter, we explain briefly the theories of laser cladding and solid state sintering.

Laser cladding is performed to improve the surface properties of metallic machine parts locally. A cladding material with the desired properties is fused onto a substrate using a laser beam. Mixing between the two materials should be minimized to use the properties of the coating material most effectively. By improving a technical surface locally with a dedicated material, one can use an ordinary, inexpensive base material for a surface that is not exposed to high loads. Laser cladding is considered a strategic technique, because it can provide surface layers that, compared with other hard-facing techniques, have superior properties in terms of purity, homogeneity, hardness, bonding, and microstructure [41, 42].

Solid-state sintering is an important method in the industrial fabrication of many ceramics. While a liquid phase may allow enhanced densification at lower temperatures, a difficulty, particularly in the case of ceramics for structural applications, is that the maximum use temperature of the material may be controlled by the softening temperature of the solidified liquid phase. Under some conditions, the densification achieved by any sintering technique may be inadequate [43]. One solution to this is the application of external energy.

6.2. Particle heating in coaxial laser

This paper deals with the modeling of the laser cladding process, paying particular attention to the phenomena of powder stream formation, power stream heating, and particle addition into the melt pool, while considering the interactions between three important elements: the laser beam, the powder stream, and the substrate. Inclusion of the substrate in the modeling domain provides the opportunity to study powder catchment in detail, which could help to further improve the efficiency of the process.

The dynamic behavior of a gas-propelled powder stream is analyzed first, considering the important phenomena of drag and wall bouncing. Then, the heating of particles is modeled using a lumped capacitance method. Interactions between the laser beam, powder stream, and substrate are also analyzed at this stage. Finally, the addition of powder particles into the melt pool is investigated for various cladding scenarios [44].

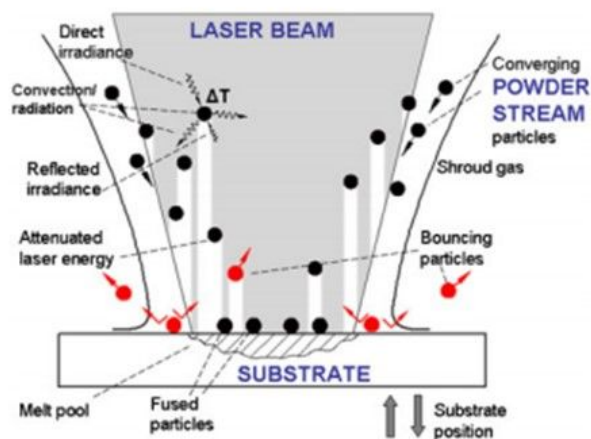


Figure 55 Map of phenomena that occur during deposition [44]

6.3. Thermal effect of laser in LaNPDS

LaNPDS mechanism is similar to laser cladding. The difference is only the flying particle influenced by laser. This system can consider the particles are heated during the flying, while at the same time particle exchange the heat with the surrounding media by convection and radiation [44]. Under these conditions, the energy balance can be described by the following relation

$$V_p \rho_p c_p \frac{dT}{dt} = I_T \eta_p \pi r_p^2 - h(T - T_\infty) 4\pi r_p^2 - \varepsilon \sigma (T^4 - T_\infty^4) 4\pi r_p^2 \quad (8).$$

Where V_p is the volume of the particle, ρ_p is the particle density, c_p is the specific heat, T is the temperature of the particle in the time t , η_p is the particle absorption coefficient, h is the heat convection coefficient, T_∞ is the temperature of the surrounding gas, ε is the particle emissivity, σ is the Stefan–Boltzman constant and I_T is the total energy incident on the particle. It is defined as $I_T = I_d + I_r$, where I_d represents the laser energy directly incident on powder particles, and follows a uniform distribution according to

$$I_d = \frac{P}{\pi [r_1(y)]^2} \quad (9)$$

Where the I_d is the energy from direct laser irradiance, P is the laser power and $r_1(y)$ is the radius of the laser beam at the y plane.

Depending on the absorptivity of the substrate, a portion of the incident energy on it will be reflected back to the surrounding media. It is assumed that this reflection will be of a diffuse nature, according to the Lambert law

$$I_r = I_{ds} (1 - \eta_s) \cos \theta d\Omega dS \quad (10)$$

Where I_{dS} is the energy incident at the surface element dS on the substrate surface, η_s is the absorption coefficient of the substrate, θ is the angle formed between the normal line to dS and the imaginary line that projects the droplet to the center of dS , Ω is the solid angle formed between the element dS and the particle.

To model the LaNPDS process, we assumed that there was no energy exchanges in the substrate. The modeling was only of an intermediate process through the deposition and flying particles. Figure 55 shows the laser energy exchange process considering only laser-beam scattering. To calculate the duration time τ , it is necessary to know the V_s . In chapter 4, the velocity of particles was determined by PIV measurement and CFD analysis.

Figure 56 shows calculated temperature of flying particles. There was difference between measured values, using a thermocouple, and theoretically calculated values. There are limits to measuring the temperature on the fast flying particles. Using a nanosecond pulsed laser can cause differences in the actual measured temperatures. Additional studies are required of this.

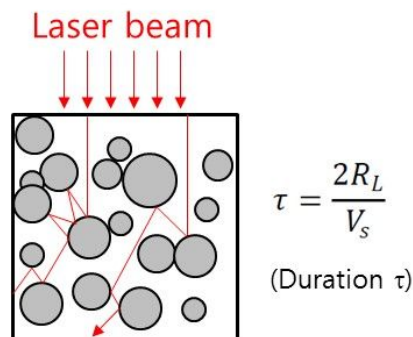


Figure 56 Schematic diagram of laser energy irradiation of flying particles

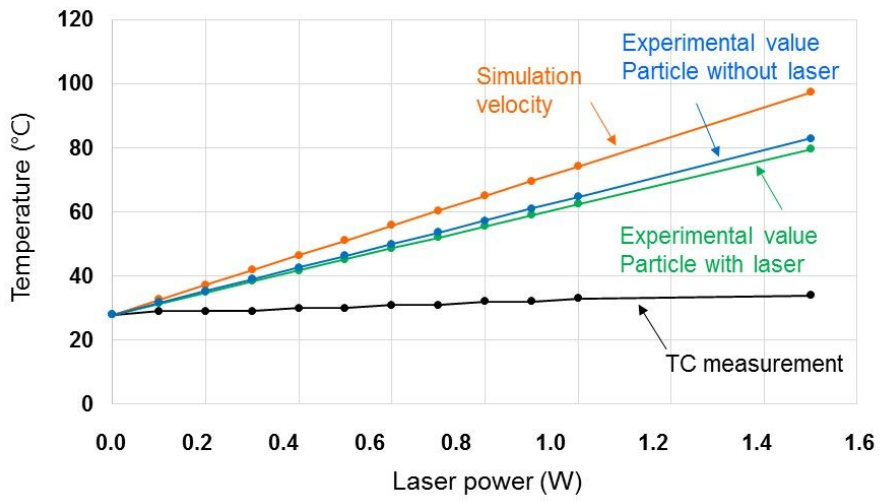


Figure 57 Calculated temperature of flying particle in a laser-assisted nanoparticle deposition system (LaNPDS)

6.4. Relationships between the kinetic energy of the particles and laser activation energy in LaNPDS

In the LaNPDS deposition process, there are two important variables: the kinetic energy and laser activation energy. The governing equations are the same as those in chapter 4 regarding computational fluid dynamics. In this chapter, we also include nozzle modeling. When passing through the nozzle, the velocity of particles increases to reach the substrate, which has a significant effect on the deposition results. Additionally, the amount of energy that the laser transmits to the flying particles until they pass through the nozzle can be calculated.

6.4.1 ANSYS modeling for particle velocity

For the CFD analysis, most commonly used nozzle and process condition was selected. The nozzle shape is described in figure 57. It is the rectangular supersonic nozzle with 1 mm × 0.4 mm exit. Inlet diameter is 10 mm.

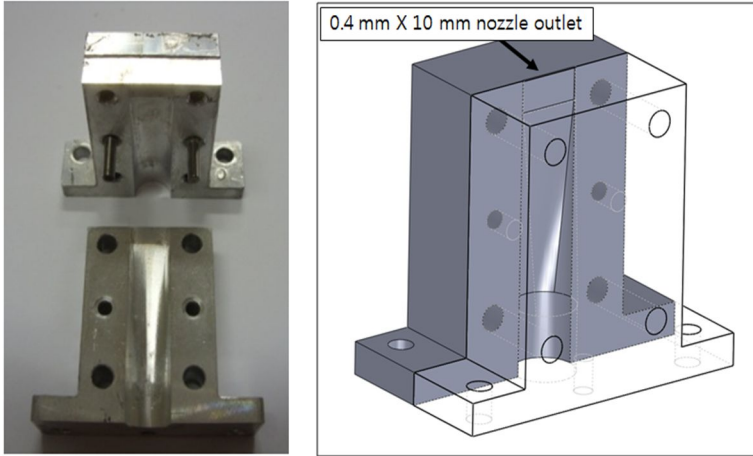


Figure 58 Image of slit shape nozzle

Figure 58 shows the nozzle inlet and surroundings such as nozzle outlet, and substrate. The stand-off distance (SoD), the distance between the nozzle exit and the substrate, is 3 mm. the pressure of the carrier gas is 0.4 MPa, and the vacuum is 0.03 MPa.

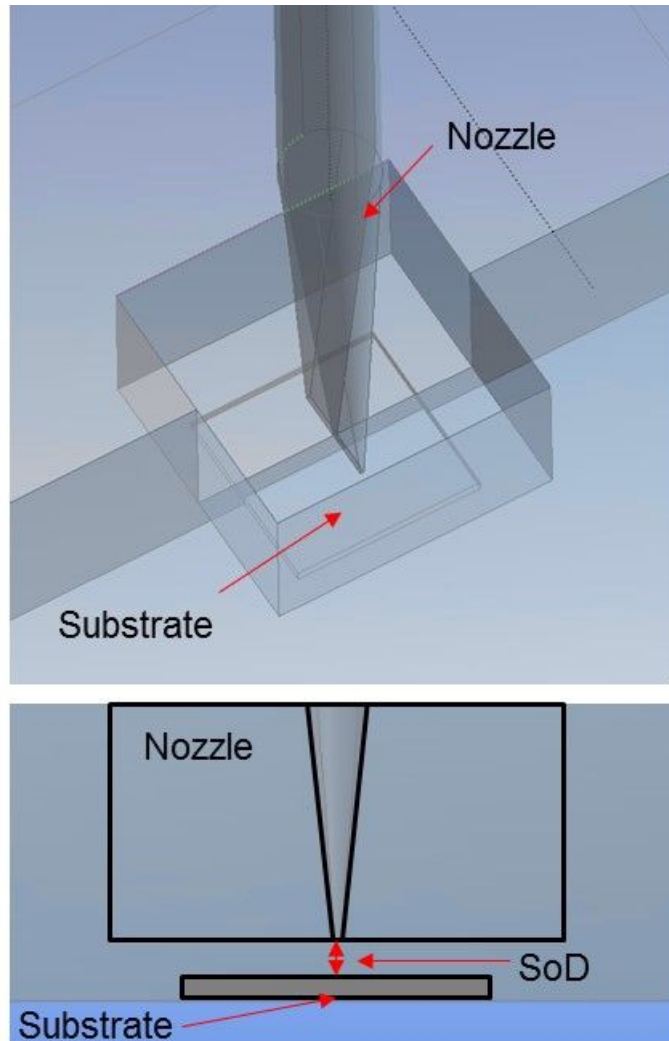


Figure 59 Geometry information of CFD analysis modeling

The particle was selected as Al_2O_3 with $1\ \mu\text{m}$ diameter. Figure 59 shows the flow and particle velocity around the nozzle. The maximum velocity of flow was $435.5\ \text{m/sec}$. Along the nozzle, the velocity of flow kept increasing, but it suddenly decreased near the substrate. The reason is shock waves ($\text{ma} = 1$). The normal shock was created near the nozzle throat, and the bow shock was created in front of the substrate.

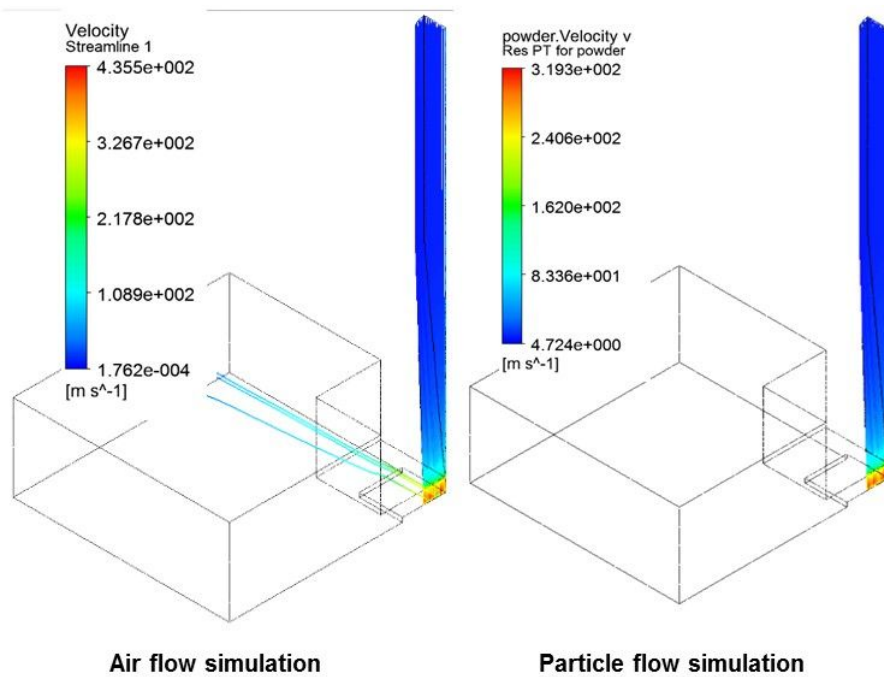


Figure 60 Contour image of CFD results about air and particle flow velocity

The velocity of Al_2O_3 particles showed a maximum of 319.3 m/sec. Overall, the particles moved along the air flow. At the substrate, the velocity of the particle is zero, because of the non-slip boundary condition. Particles were accelerated through the nozzle and outside the nozzle, because of the drag force due to the difference in velocity between the particle and air flow, and the pressure gradient.

Figure 60 shows the velocity result of air flow and particle from the nozzle inlet to substrate. The length of inside of nozzle is 80 mm and stand-off distance (SoD) is 3 mm. The total length of air and particle flow 83 mm as shown.

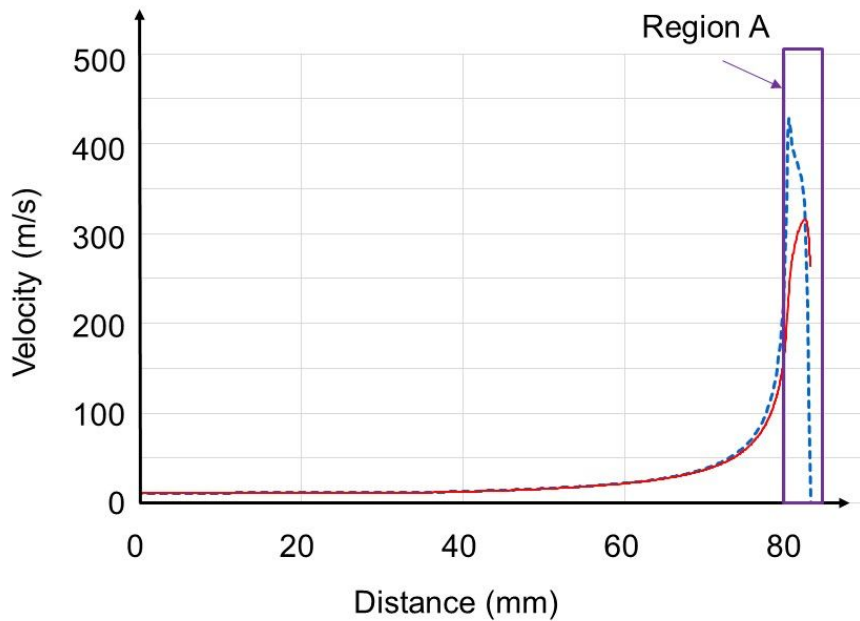


Figure 61 Velocity result of computational fluid dynamics (CFD) analysis

In Figure 61, the picture shows region A in detail. After the nozzle outlet, the velocity of air flow is faster than that of particles. However, near the substrate, the velocity of the air flow is slower than the particles.

This result shows that the important issue is not the velocity of the particle in flight, but the real impact velocity of the particle.

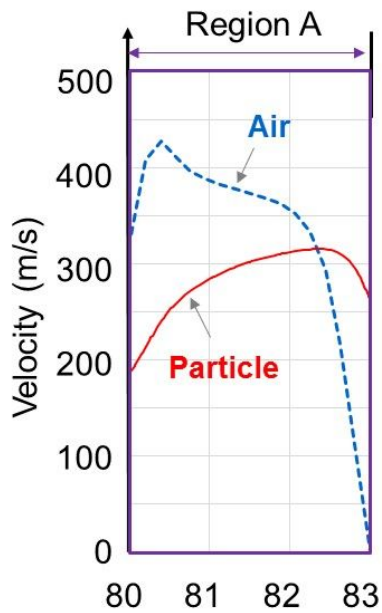


Figure 62 Velocity result of CFD analysis in region A

6.4.2 Laser activation energy

To describe the effects of the laser sintering, the theory of the diffusion of the material needs to be understood. For the case of Al_2O_3 particles, the major diffusion processes of $\alpha\text{-Al}_2\text{O}_3$ have been reviewed, including oxygen and aluminum lattice diffusion [45]. There have also been many studies aimed at finding the mechanism of the sintering process, in terms of the kinetic and activation energies [46-48].

The activation energy is determined by the size of the particle, the heat transfer coefficient, and the density and phase of the material. For a surface diffusion and sintering effect, the particle must obtain the basic activation energy. Table 7 shows activation energies for the $\alpha\text{-Al}_2\text{O}_3$. For the same phase of a particle, a larger particle needs more activation energy. When the particle size is 100–150 nm, the activation energy was 120.2 kJ/mol, and a particle of 1 μm needs 541.1 kJ/mol.

Table 6 Activation energy of Al_2O_3 particles in sintering conditions

	<i>Ref 1)</i>	<i>Ref 2)</i>	LaNPDS
Particle size	100 – 150 nm	About 1 μm	About 1 μm
Activation energy (kJ/mol)	120.2	541.1	786.75

In LaNPDS, the energy from the laser can be calculated with the following equations (3D diffusion; Ginstling and Brounshtein). The amount of energy calculated is 786.75 kJ/mol. Many assumptions were made and the formulae were simplified, so this may not be sufficiently accurate to describe practical phenomena. However, the value can be used to understand the grounds for a sintering effect occurring with LaNPDS.

$$k(T) = A \exp\left(-\frac{E\alpha}{RT}\right) \quad (11)$$

$$\ln k(T) = \ln A + \left(-\frac{E\alpha}{R}\right)\left(\frac{1}{T}\right) \quad (12)$$

$$f(\alpha) = 3/\{2[(1 - \alpha)^{-\frac{1}{3}} - 1]\} \quad (13)$$

6.4.3 Comparison of kinetic energy and laser activation energies

Figure 62 shows the kinetic energy and laser activation energy. Before the nozzle outlet, activation energy from the laser was higher than kinetic energy from the flying particles. After exiting of the nozzle outlet, the particle's kinetic energy increased markedly. However, as explained earlier, the particle velocity was decreased near the substrate by bow shock.

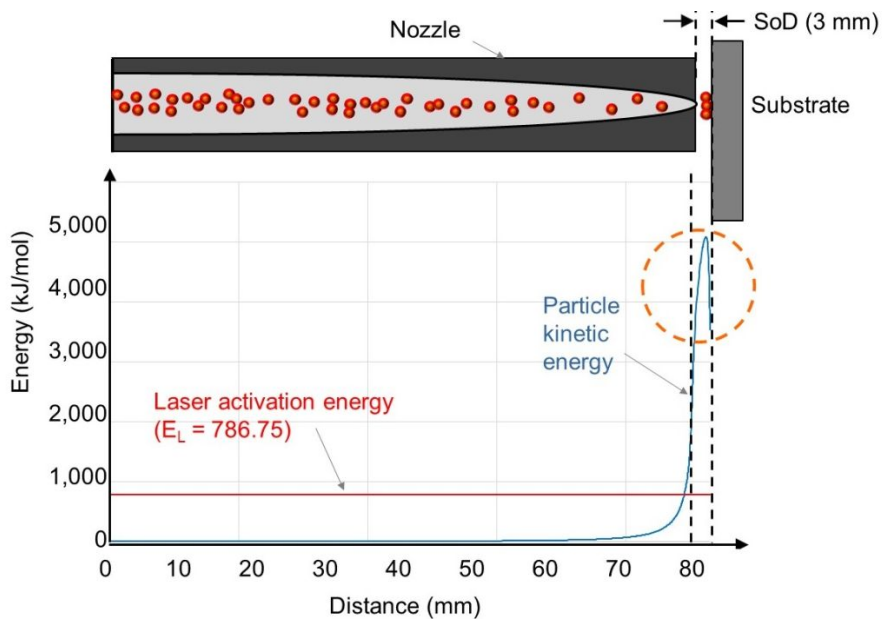


Figure 63 Kinetic energy and laser activation energies

Figure 63 shows more detailed information about the particle kinetic energy and laser activation energy. To facilitate a comparison of the kinetic and activation energies, both are presented in kJ/mol. The maximum kinetic energy was 5,085.72 kJ/mol. At the substrate, it had decreased to 3,547.37 kJ/mol.

The laser activation energy is assumed to initially to keep the energy, 786.75 kJ/mol, received by the laser. The ratio of the kinetic energy to the particle, and the activation energy at the moment the particle reaches the substrate, is 1:4.52 for this assumption.

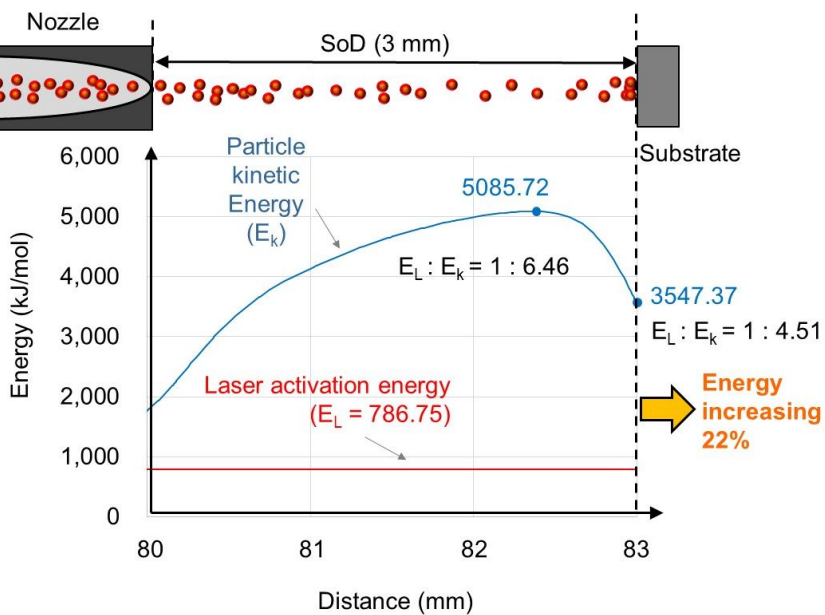


Figure 64 Comparison of kinetic and laser activation energies beyond the nozzle outlet

Chapter 7 Conclusions

Novel LaNPDS hybrid manufacturing equipment was designed and developed by integrating the NPDS with a 355-nm pulsed laser. Exploiting the beneficial properties of both processes and taking advantage of room-temperature processing, decreased thermal damage and sintering-effect deposition were implemented using the processes simultaneously in a cost-effective manner.

The deposition of ceramic and metal powder at room temperature was achieved using appropriate combinations of process parameters. For ceramic deposition, TiO_2 and Al_2O_3 were deposited on ceramic and polymer substrates, and the material properties of the resulting deposition were analyzed. In conclusion, laser assistance significantly improved the surface properties (hardness and modulus, due to the enhanced particle bonding force) of the substrates. The surface morphologies, cross-sections, chemical composition, crystallographic structures, and mechanical properties of TiO_2 films were characterized by various surface analytical methods, including FE-SEM, SIM, energy dispersive X-ray spectroscopy (EDXS), XRD, and nano-indentation.

As an example application, DSSCs were fabricated by depositing TiO_2 nanoparticles as a semiconductor oxide layer on glass and polymer substrates. The deposition of TiO_2 nanoparticles on both substrates was achieved successfully. LaNPDS can deposit nanoparticles on polymer substrates, such as those used in flexible solar cells, and increase the solar energy conversion efficiency according to the closely packed nanoparticle structure-based thin film with no additional thermal sintering process (unlike previous laser-assisted processes and NPDS).

Effects of the laser on flying particles were suggested, based on the laser cladding theory. This has not yet been solved computationally, but the conditions of flying particles and air flow were measured experimentally and

compared with a CFD analysis.

To describe the effects of the laser sintering, the theory of the diffusion of the material needs to be understood. For the case of Al_2O_3 particles, kinetic and activation energies were considered to finding the mechanism of the sintering process.

Before the nozzle outlet, activation energy from the laser was higher than kinetic energy from the flying particles. After exiting of the nozzle outlet, the particle's kinetic energy increased markedly. However, as explained earlier, the particle velocity was decreased near the substrate by bow shock. The ratio of the kinetic energy to the particle, and the activation energy at the moment the particle reaches the substrate, is 1:4.52 for this assumption.

Bibliography

- [1] Chun, D.M., et al., TiO₂ coating on metal and polymer substrates by nano-particle deposition system (NPDS). *CIRP Annals - Manufacturing Technology*, 2008. 57(1): p. 551-554.
- [2] Chun, D.M., et al. Nano particle deposition system (NPDS) for ceramic and metal coating at room temperature and low vacuum condition. in *Smart Manufacturing Application*, 2008. ICSMA 2008. International Conference on. 2008.
- [3] Doo-Man, C., et al., Nano/micro particle beam for ceramic deposition and mechanical etching. *Physica Scripta*, 2010. 2010(T139): p. 014047.
- [4] Chagnon, P. and P. Fauchais, Thermal spraying of ceramics. *Ceramics International*, 1984. 10(4): p. 119-131.
- [5] Sasaki, Y., et al., The Fourth International Conference on Nanostructured Materials (NANO '98) 3D transition ferromagnetic metal nano-crystals prepared with gas deposition method (GDM). *Nanostructured Materials*, 1999. 12(5): p. 907-910.
- [6] Rao, N.P., et al., Hypersonic plasma particle deposition of nanostructured silicon and silicon carbide. *Journal of Aerosol Science*, 1998. 29(5-6): p. 707-720.

- [7] Svavarsson, H.G., et al., Electrostatic powder impact deposition (EPID) of Ge on Si and Cu substrates, microstructure and morphology study. *Journal of Physics D: Applied Physics*, 2000. 33(10): p. 1155.
- [8] Papyrin, A., Kosarev, V., Klinkov, S., Alkimov, A. and Fomin, V. , Cold spray technology. 2007, Oxford: Elsevier.
- [9] Akedo, J., Aerosol Deposition of Ceramic Thick Films at Room Temperature: Densification Mechanism of Ceramic Layers. *Journal of the American Ceramic Society*, 2006. 89(6): p. 1834-1839.
- [10] Jun, A. and L. Maxim, Microstructure and Electrical Properties of Lead Zirconate Titanate ($\text{Pb}(\text{Zr}_{52}/\text{Ti}_{48})\text{O}_3$) Thick Films Deposited by Aerosol Deposition Method. *Japanese Journal of Applied Physics*, 1999. 38(9S): p. 5397.
- [11] Akedo, J., Room Temperature Impact Consolidation (RTIC) of Fine Ceramic Powder by Aerosol Deposition Method and Applications to Microdevices. *Journal of Thermal Spray Technology*, 2008. 17(2): p. 181-198.
- [12] Griffith, M.L. and J.W. Halloran, Freeform Fabrication of Ceramics via Stereolithography. *Journal of the American Ceramic Society*, 1996. 79(10): p. 2601-2608.
- [13] Dahotre, N.B. and S. Harimkar, Laser Fabrication and Machining of Materials. 1 ed. 2008, Springer-Verlag US: Springer US.

- [14] Kruth, J.P., et al., Lasers and materials in selective laser sintering. *Assembly Automation*, 2003. 23(4): p. 357-371.
- [15] K. Y. Park, a.K.Y.J., Synthesis of nano-structured aluminapowders thru the aerosol process. *Ceramist*, 2009. 12(2): p. 11.
- [16] Booth, G., R. Jones, and P. Threadgill. Recent Developments in Welding Technology. in *The Sixteenth International Offshore and Polar Engineering Conference*. 2006. International Society of Offshore and Polar Engineers.
- [17] Griffith, M., et al. Free form fabrication of metallic components using laser engineered net shaping (LENS). in *Proceedings of the Solid Freeform Fabrication Symposium*. 1996. University of Texas at Austin Austin, TX.
- [18] Process for Producing Nano-Alpha-Alumina Powder. *ISRN Nanotechnology*, 2011.
- [19] Lee, G.W., Phase transition characteristics of flame-synthesized gamma- Al_2O_3 nanoparticles with heat treatment. *Int. J. Chem. Nucl. Metall. Mater. Eng*, 2013. 7(9): p. 358-361.
- [20] Kim, J., J. Kim, and M. Lee, Laser welding of nanoparticulate TiO_2 and transparent conducting oxide electrodes for highly efficient dye-sensitized solar cell. *Nanotechnology*, 2010. 21(34): p. 345203.

- [21] Kim, H., et al., Laser-sintered mesoporous TiO₂ electrodes for dye-sensitized solar cells. *Applied Physics A*, 2006. 83(1): p. 73-76.
- [22] Pan, H., et al., Laser annealed composite titanium dioxide electrodes for dye-sensitized solar cells on glass and plastics. 2009.
- [23] Black, D.L., M.Q. McQuay, and M.P. Bonin, Laser-based techniques for particle-size measurement: a review of sizing methods and their industrial applications. *Progress in Energy and Combustion Science*, 1996. 22(3): p. 267-306.
- [24] Inaba, K. and K. Matsumoto, The development of the measurement of particle concentration using a commercial laser diffraction particle size analyzer. *Advanced Powder Technology*, 1999. 10(1): p. 89-103.
- [25] Kinoshita, T., The method to determine the optimum refractive index parameter in the laser diffraction and scattering method. *Advanced Powder Technology*, 2001. 12(4): p. 589-602.
- [26] Doudou, A., Turbulent flow study of an isothermal diesel spray injected by a common rail system. *Fuel*, 2005. 84(2): p. 287-298.
- [27] Du, L., J.Z. Yao, and W. Lin, Experimental study of particle flow in a gas–solid separator with baffles using PDPA. *Chemical Engineering Journal*, 2005. 108(1): p. 59-67.

- [28] Ji, H.J.W.H.M., Study on velocity field in hydrocyclone model by PDPA measurement [J]. Chinese Journal of Environmental Engineering, 2010. 5: p. 029.
- [29] Van den Moortel, T., et al., Experimental analysis of the gas-particle flow in a circulating fluidized bed using a phase Doppler particle analyzer. Chemical Engineering Science, 1998. 53(10): p. 1883-1899.
- [30] Kumara, W., et al., Comparison of Particle Image Velocimetry and Laser Doppler Anemometry measurement methods applied to the oil-water flow in horizontal pipe. Flow measurement and Instrumentation, 2010. 21(2): p. 105-117.
- [31] Kashyap, M., B. Chalermssinsuwan, and D. Gidaspow, Measuring turbulence in a circulating fluidized bed using PIV techniques. Particuology, 2011. 9(6): p. 572-588.
- [32] Sarkar, D., et al., In situ particle size estimation for crystallization processes by multivariate image analysis. Chemical Engineering Science, 2009. 64(1): p. 9-19.
- [33] Othman, N.T.A., H. Obara, and M. Takei, Cross-sectional capacitance measurement of particle concentration in a microchannel with multi-layered electrodes. Flow Measurement and Instrumentation, 2013. 31: p. 47-54.

- [34] Li, W., et al. Impact fusion of particle interfaces in cold spraying and its effect on coating microstructure. in Thermal Spray 2007: Global Coating Solutions: Proceedings of the 2007 International Thermal Spray Conference. 2007. ASM International.
- [35] ANSYS, Inc. : <http://www.ansys.com>.
- [36] O'regan, B. and M. Grfitzeli, A low-cost, high-efficiency solar cell based on dye-sensitized. nature, 1991. 353(6346): p. 737-740.
- [37] Rani, S., P. Suri, and R.M. Mehra, Mechanism of charge recombination and IPCE in ZnO dye-sensitized solar cells having I⁻/I₃⁻ and Br⁻/Br₃⁻ redox couple. Progress in Photovoltaics: Research and Applications, 2011. 19(2): p. 180-186.
- [38] Kim, M.-S., et al., Room temperature deposition of TiO₂ using nano particle deposition system (NPDS): Application to dye-sensitized solar cell (DSSC). International Journal of Precision Engineering and Manufacturing, 2011. 12(4): p. 749-752.
- [39] Zhang, D., et al., Low-temperature preparation of amorphous-shell/nanocrystalline-core nanostructured TiO₂ electrodes for flexible dye-sensitized solar cells. Journal of Nanomaterials, 2008. 2008: p. 66.
- [40] Park, S.-I., et al., Low-cost fabrication of WO₃ films using a room temperature and low-vacuum air-spray based deposition system for inorganic electrochromic device applications. Thin Solid Films, 2015. 589: p. 412-418.

- [41] Lin, J. and W.M. Steen. Powder flow and catchment during coaxial laser cladding. in Lasers and Optics in Manufacturing III. 1997. International Society for Optics and Photonics.
- [42] Vilar, R., Laser cladding. Journal of Laser Applications, 1999. 11(2): p. 64-79.
- [43] Monteiro, S. and C. Vieira, Solid state sintering of red ceramics at lower temperatures. Ceramics International, 2004. 30(3): p. 381-387.
- [44] Ibarra-Medina, J. and A.J. Pinkerton, Numerical investigation of powder heating in coaxial laser metal deposition. Surface Engineering, 2011. 27(10): p. 754-761.
- [45] Heuer, A., Oxygen and aluminum diffusion in α -Al₂O₃: how much do we really understand? Journal of the European Ceramic Society, 2008. 28(7): p. 1495-1507.
- [46] Fang, T.-T., J.-T. Shiue, and F.-S. Shiau, On the evaluation of the activation energy of sintering. Materials chemistry and physics, 2003. 80(1): p. 108-113.
- [47] Holková, Z., et al., Kinetic study of Al₂O₃ sintering by dilatometry. Ceramics-Silikáty, 2003. 47(1): p. 13-19.
- [48] Park, K., et al., Size-resolved kinetic measurements of aluminum nanoparticle oxidation with single particle mass spectrometry. The journal of physical chemistry B, 2005. 109(15): p. 7290-7299.

초 록

건식 나노입자분말적층장치와 레이저를 결합하여 새로운 하이브리드 공정(LaNPDS)을 제작하였다. 제시된 새로운 방식의 장비는 기존 나노입자분말적층장치의 장점(상온, 저진공 조건에서 세라믹과 금속 분말의 적층 가능)을 그대로 유지하며, 레이저를 사용하여 추가적인 에너지를 날아가는 분말에 전달하여 보다 기계적 물성이 우수한 적층 결과를 얻을 수 있도록 하였다.

기존의 레이저 에너지를 사용하는 연구들의 경우 레이저가 기관에 조사되며, 분말을 녹이기 위하여 높은 에너지를 가지는 레이저를 사용한다. 때문에 기관에 열 손상이 가해지고, 폴리머, 전도성 필름 등 열에 약한 기관의 선택에 제약을 받게 된다. 또한 3-D 프린터와 같은 3차원형상을 제작을 연구목표로 하고 있어 대면적으로 활용하기에 한계점을 지닌다.

본 연구에서는 분말이 날아가는 중에 레이저와 에너지를 교환하도록 하는 새로운 방식의 하이브리드 장비를 제시하였다. 직접 설계 및 제작된 레이저와 건식 분말 적층 장치를 사용한 하이브리드 공정의 경우 노즐 이후에는 레이저의 영향을 제거 함으로써 기관에 열 영향 없이 세라믹과 금속 분말을 적층할 수 있다. 이 같은 공정을 사용하는 경우 기존의 나노입자분말적층장치 보다 기계적 물성이 우수한 적층 결과를 얻을 수 있었다.

날아가는 분말에 미치는 레이저의 영향은 열로 인한 소결효과와 유사한 양상을 보인다. 이 때 레이저의 영향을 파악하기 위하여 SEM, TEM, XRD 등의 실험을 통하여 적층된 분말의 기계적 물리적 특성을 확인하였다. 또한 유체역학과 유한요소법을 사용하여 분말의

이동 속도를 해석하였고, 이를 검증하기 위하여 CCD 카메라를 사용한 Zn 분말의 속도 측정을 수행하였다.

노즐을 통과하여 적층되는 분말은 레이저로부터 에너지를 받는 동시에 유체의 흐름에 따라 가속되어 운동에너지를 지니게 된다. 본 연구에서는 날아가는 분말이 가지는 운동에너지와 레이저를 통하여 얻게 되는 에너지를 비교하고, 이를 통하여 보다 효율적이고 양질의 적층 결과를 확보할 수 있는 새로운 형태의 공정을 개발하였다.

주요어 : 나노입자분말적층장치, 건식 분사적층, 레이저, 하이브리드 시스템

학 번 : 2010-20725